Manuscript title:

Mapping protein distribution in the canine photoreceptor sensory cilium and calyceal processes by ultrastructure expansion microscopy

Authors and affiliations:

Kei Takahashi[1], Raghavi Sudharsan[1], William A. Beltran[1] *

[1]Division of Experimental Retinal Therapies, Department of Clinical Sciences & Advanced Medicine, School of Veterinary Medicine, University of Pennsylvania, Philadelphia, PA 19104

***Correspondence**: William A. Beltran, Division of Experimental Retinal Therapies, Department of Clinical Sciences & Advanced Medicine, School of Veterinary Medicine, University of Pennsylvania, 3900 Delancey Street, Philadelphia, PA, 19104, USA. Email: wbeltran@vet.upenn.edu

Keywords

Canine retina, Connecting cilium, Calyceal processes, Photoreceptor sensory cilium, Ultrastructure expansion microscopy

Abstract

Photoreceptors are highly polarized sensory neurons, possessing a unique ciliary structure known as the photoreceptor sensory cilium (PSC). Vertebrates have two subtypes of photoreceptors: rods, which are responsible for night vision, and cones, which support daylight vision and color perception. Despite identifying functional and morphological differences between these subtypes, ultrastructural analyses of the PSC molecular architecture in rods and cones are still lacking. In this study, we employed ultrastructure expansion microscopy (U-ExM) to characterize the molecular architecture of the PSC in canine retina. We demonstrated that U-ExM is applicable to both non-frozen and cryopreserved retinal tissues with standard paraformaldehyde fixation. Using this validated U-ExM protocol, we revealed the molecular localization of numerous ciliopathy-related proteins in canine photoreceptors. Furthermore, we identified significant architectural differences in the PSC, ciliary rootlet, and calyceal processes between canine rods and cones. These findings pave the way for a better understanding of alterations in the molecular architecture of the PSC in canine models of retinal ciliopathies.

Introduction

Photoreceptors are highly polarized sensory neurons, located in the outermost layer of the neuroretina that play a crucial role in light detection and signal transduction. In vertebrate retinas, there are two subtypes of photoreceptors: rods, which are highly sensitive to light and essential for night vision, and cones, which provide high visual acuity, color perception, and daylight vision [1]. These cells possess a unique sensory ciliary structure known as the photoreceptor sensory cilium (PSC). Within the PSC, photoreception and phototransduction occur in the outer segment (OS), a highly elaborated membrane structure supported by a nine-fold microtubule axoneme that originates from the basal body (BB) in the inner segment (IS). The region connecting the OS and IS, termed the connecting cilium (CC), is characterized by Y-shaped linkers (Y-links) that anchor each microtubule axoneme to the cell membrane and function as a critical gateway for ciliary trafficking [2, 3] (**Figure 1**). These fundamental features of the tubulin-based PSC architecture are thought to be shared between rods and cones, although detailed structural analyses for cone PSC are still lacking [4].

Using cryo-electron tomography, the ultrastructure of rod PSC has been thoroughly analyzed in the mouse retina, revealing that the CC structure of mouse rods is approximately 1.1 μm in length and 300 nm in diameter [5]. Additionally, immunogold electron microscopy has been employed to investigate the precise localization of proteins within this small subcellular compartment, identifying the distribution of several ciliary proteins in mouse rod PSC [6-8]. However, despite the identification of pathogenic variants in over 50 genes associated with non-syndromic retinal ciliopathies [9], the specific roles and precise distribution of these proteins within the PSC have remained largely uncharacterized due to the limited resolution and detection capabilities of conventional fluorescence immunohistochemistry.

With recent advances in super-resolution imaging techniques, it has become feasible to analyze detailed protein localization and morphology within the PSC using fluorescence immunostaining [10-13]. Notably, expansion microscopy (ExM), a sample preparation-based approach in which the specimen is expanded with a swellable hydrogel polymer and allows for ultrastructure observation without the need for specialized microscopy equipment, has become widely accessible to researchers [14]. Numerous

59 modified ExM protocols have been developed to optimize imaging for specific subcellular compartments
60 and sample conditions [15], some of which have been successfully applied to investigate the
61 ultrastructure of photoreceptors [16-18]. Among these advanced methods, ultrastructure expansion
62 microscopy (U-ExM) is particularly notable for its ability to preserve the native intracellular architecture of
63 biological specimens while enabling nanometer-scale observation using standard primary and secondary
64 antibodies used in immunohistochemistry [19]. U-ExM has already made significant contributions to the
65 molecular mapping of the mouse PSC and the detailed assessment of AAV-based gene augmentation
66 therapy in mouse retinal ciliopathy models [18, 20, 21].

67 Mice are frequently employed in research on PSC morphology and inherited retinal diseases (IRDs),
68 including retinal ciliopathies, due to their ease of handling, low breeding costs, and suitability for gene
69 editing. However, there are significant functional and structural differences between rodent and human
70 photoreceptors, such as very low percentage of cones, the absence of a foveomacular region, and the
71 lack of calyceal processes [22-24]. To address these limitations and enhance the relevance of preclinical
72 animal models, large animals such as dogs, cats, and pigs are proving to be valuable IRDs models.
73 Notably, canine models hold promise for advancing our understanding of the pathogenic mechanisms of
74 IRDs, owing to their fovea-like cone-rich structure [25] and the identification of an increasing number of
75 naturally-occurring genetic mutations linked to human IRDs [26]. Despite this potential, detailed
76 morphological studies on canine photoreceptors remain limited. In this study, we utilize U-ExM to
77 characterize the molecular architecture of the normal adult canine PSC. We validate the U-ExM method
78 for long-term cryopreserved canine retinal samples and provide a comprehensive analysis of the
79 architectural features of the canine PSC. This includes differences in PSC structure between rods and
80 cones, the distribution of retinal ciliopathy-related proteins, and the presence or absence of calyceal
81 processes.

Results

U-ExM protocol is effective on non-frozen and cryopreserved canine retinal tissues

To investigate whether U-ExM could be applied to canine retinal tissues, we tested a U-ExM protocol recently adapted for mouse retina [18] on adult canine retinal tissues subjected to different fixation and storage conditions. The short fixation condition (4% paraformaldehyde (PFA) for 15 minutes) is the same as that used for mouse retina in the previous U-ExM study, while a longer fixation protocol (4% PFA for 3 hours followed by 2% PFA for 24 hours) is routinely used by our lab for long-term cryopreservation of canine retinal tissues.

First, we assessed the structural preservation of the photoreceptor OS after expansion under each sample condition. In non-frozen retinas fixed for the short duration, the OS were severely damaged and unevenly swollen (**Figure 2A**). In contrast, the OS structures of both rods and cones were better preserved in the retinas fixed for the longer duration (**Figure 2B**). Similarly, the OS of the cryosection-derived U-ExM samples exhibited relatively better preservation compared to the short-fixed non-frozen retina, although they showed mild damage (**Figure 2C**). Since slight damage to the OS structure was observed even in the unexpanded cryosections (**Figure 2D**), it is likely that the quality of the cryosectioning was reflected in the sample after expansion.

Next, to verify whether the expansion factor was affected by fixation duration and storage conditions in canine retinal tissues, we compared the structure of the tubulin axoneme of the PSC under each sample condition. Although non-acetylated tubulin has frequently been used as a PSC axoneme marker in previous U-ExM studies using mouse retina [18, 20, 21], this labeling also showed a distinct signal in the photoreceptor IS. In contrast, immunostaining with antibodies targeting acetylated α-tubulin (AcTub), a widely used marker of primary cilia, labeled the PSC axoneme with high specificity (**Figure 2E**). Furthermore, labeling of acetylated and non-acetylated tubulin at the BB and CC of the PSC showed identical localization in the magnified images of the U-ExM samples, though the non-acetylated tubulin signal was more prominent in the distal axoneme (**Figure 2F-H**). This might suggest that the distal part of the PSC is less prone to acetylation than the BB and CC. We employed AcTub as a highly specific

108 marker for the PSC axoneme in subsequent studies. The width of the AcTub-labeled axoneme on the CC
109 and the proximal end of the BB after processing by U-ExM was comparable across all sample conditions
110 (**Figure 2J and K**). By dividing the CC axoneme width of U-ExM samples by 200.84 nm, which is the
111 previously reported CC axoneme width of mouse photoreceptors [5], we determined an average
112 expansion factor of 3.83 across all sample conditions. Similarly, the gel diameter immediately after the
113 first-round of expansion reached approximately 5 cm in all sample conditions (**Supplementary Figure**
114 **2I**), averaging a 4.17 times larger dimension than the original gel diameter. These values are not notably
115 different from the typical expansion factor (~4) reported in previous U-ExM studies [18, 19].
116 We further investigated the localization patterns of representative CC-associated proteins to verify
117 whether there are differences in the localization of these proteins among the different sample conditions.
118 Centrin and CEP290 (NPHP6), which have been well characterized in mouse photoreceptors as the CC
119 inner scaffold protein and Y-link-associated protein, respectively [18], were examined. In U-ExM
120 processed canine photoreceptors, Centrin localized specifically inside the tubulin axoneme of the BB and
121 CC (**Figure 2L-N**), while CEP290 was observed outside the CC axoneme (**Figure 2P-R**), consistent with
122 their previously reported localization patterns. Moreover, there were no significant differences in the
123 localization of these proteins among the different sample conditions. In summary, our findings confirmed
124 that U-ExM could be utilized for canine retinal tissue and that variations in PFA fixation and storage
125 conditions do not affect the expansion factor. Considering the better preservation of OS structure, we
126 used long-fixed non-frozen retinas and frozen archival retinal tissues for the subsequent studies
127 described below.
128
129 **Differences in tubulin-based molecular architecture between rod and cone PSC**
130 We then analyzed the molecular architecture of the tubulin axoneme in rod and cone PSC of normal
131 adult canine retinas processed by U-ExM. Rod and cone photoreceptors were distinguished by labeling
132 with rhodopsin and cone arrestin (CAR), respectively. The tubulin axoneme in both photoreceptor
133 subtypes was visualized by labeling acetylation and glutamylation on the tubulin, which are well-known

134 post translational modifications in the centriole and primary cilium, using AcTub and GT335 antibodies.
135 In both photoreceptor subtypes, glutamylation was detected on the tubulin axoneme throughout the PSC,
136 similar to acetylation. The glutamylation signal was also found outside the tubulin axoneme only around
137 the CC region (**Figure 3A-D**). A recent study suggested that glutamylation signal shows localization
138 comparable to CEP290 in mouse photoreceptor CC [18]. Similarly, we identified that the region of the
139 glutamylation signal on the tubulin axoneme matches the CEP290 signal on the CC in canine
140 photoreceptors (**Supplementary Figure 3**). Based on these findings, we assumed that the region with
141 glutamylation outside the tubulin axoneme is equivalent to the CC and measured the length and width of
142 each compartment of the PSC axoneme (**Figure 3E**). As previously reported for other cell types [27, 28],
143 the length of the BB was significantly longer than that of the daughter centriole (DC) in each photoreceptor
144 subtype. More interestingly, cone photoreceptors had notably longer DC and BB than rods (Rod DC,
145 269.71 ± 24.00 μm; Cone DC, 357.27 ± 37.26 μm; Rod BB, 372.06 ± 55.22 μm; Cone BB, 465.84 ± 40.58
146 μm; **Figure 3F**). In contrast, the length of the CC in cones was significantly shorter than that in rods (Rod
147 CC, 1362.81 ± 164.22 μm; Cone CC, 900.35 ± 169.02 μm; **Figure 3H**). The width of the AcTub-labeled
148 tubulin axoneme in the CC, DC, and BB was identical among the photoreceptor subtypes (**Figure 3G**
149 **and I**).

150 Next, we focused on the differences between rod and cone tubulin structures in the outer region of
151 the CC, referred to as the bulge region. Based on the measurement method used in previous studies on
152 mouse photoreceptors [18, 21], we measured the width of the tubulin axoneme at multiple positions along
153 the CC in rod and cone photoreceptors: at the distal end of the CC (0), as well as 500 and 1000 nm
154 above (+500, +1000) and 500 nm below (-500) (**Figure 3J and K**). In the rod PSC, the width of the tubulin
155 axoneme significantly increased from the end of the CC to the +500 nm, then decreased to the +1000
156 nm (**Figure 3L**). Conversely, in the cone PSC, the enhanced width of tubulin axoneme from the CC
157 endpoint to the +500 nm was maintained even at the +1000 nm (**Figure 3M**). When comparing the
158 axoneme width between rods and cones at each measurement point, the cone axoneme was significantly
159 wider than the rod axoneme at all points except the middle part of the CC (-500) (**Figure 3N**). These

160 results revealed that cone photoreceptors have longer and wider bulge region than rod photoreceptors.

161

162 **Molecular mapping of the bulge region and distal axoneme in canine rod and cone PSC**

163 To further characterize the differences in molecular architecture at the distal part of the tubulin
164 axoneme between rods and cones in detail, we investigated the location of several proteins associated
165 with the bulge region and distal axoneme in both rods and cones. LCA5 (lebercilin) has been identified
166 as a bulge region-specific protein in mouse photoreceptors [18, 21]. Consistent with the results from
167 previous studies, LCA5 showed specific localization to the inner side of the bulge region in both rod and
168 cone photoreceptors in the canine PSC (**Figure 4A and B**). Additionally, RP1, known to localize from the
169 bulge region to the distal axoneme in mouse photoreceptors [21], exhibited a comparable localization
170 pattern in canine rod and cone photoreceptors (**Figure 4C and D**). In this study, we identified CCDC66
171 as a novel protein that specifically localizes to the distal axoneme of both rods and cones (**Figure 4E and**
172 **F**). CCDC66 is a microtubule-binding protein, and dysfunction of its gene has been reported to cause
173 retinal degeneration in both canine and mouse models [29-31]. While CCDC66 has been shown to
174 localize to the BB and tubulin axoneme in cell lines [32], its distribution patterns in vertebrate retinal
175 tissues have been inconsistent, with reports indicating localization in the OS and IS (**Supplementary**
176 **Table 5**). In the present study, we tested three commercially available anti-CCDC66 antibodies, including
177 those used in previous studies, on non-expanded canine retinas and found that their reactivity varied
178 significantly (**Supplementary Figure 4A, C, and E**). However, in U-ExM samples, two of the three
179 antibodies (PA5-60642 and sc-102418) produced specific signals on the PSC axoneme (**Supplementary**
180 **Figure 4B, D, and F**). Although the sc-102418 antibody exhibited more extensive labeling than PA5-
181 60642, both antibodies consistently showed a weak signal near the BB and a prominent signal at the
182 distal axoneme.

183 To elucidate the positional relationship of these three proteins in the distal part of the PSC axoneme,
184 we performed co-immunostaining of RP1 with LCA5 and CCDC66, respectively. In both rods and cones,
185 LCA5 localized slightly more basally than RP1, and these two proteins did not co-localize (**Figure 4G**

186 **and H**). Additionally, axial view images showed that LCA5 localized on the tubulin axoneme while RP1
187 localized outside the axoneme (**Figure 4I**). CCDC66 appeared to overlap with RP1 in the distal axoneme
188 in the lateral view (**Figure 4J and K**). However, in the axial view, CCDC66 was localized on the tubulin
189 axoneme, distinct from the localized area of RP1 (**Figure 4L**). By measuring the distance from the
190 proximal end of the BB to the starting point of each signal, we found that in cones, LCA5 and RP1
191 localized more basally compared to rods, while CCDC66 localized more distally (**Figure 4M**). Taken
192 together, LCA5, RP1, and CCDC66 each exhibited unique localization patterns in the distal part of the
193 PSC, and differences in localization of these proteins between rods and cones coincided with the
194 architectural differences in the bulge region between these photoreceptor subtypes (**Figure 4N**).
195

196 **Molecular mapping of the connecting cilium in canine rod and cone PSC**

197 Next, we compared the localization of CC-related proteins between rods and cones. POC5, Centrin,
198 and FAM161A have been well-characterized to localize inside the tubulin axoneme as inner scaffold
199 proteins at the BB and CC in mouse photoreceptors [18]. Consistent with the reports in mouse
200 photoreceptors, these three inner scaffold proteins exhibited internal localization within the axoneme at
201 the BB and CC in both canine photoreceptor subtypes (**Figure 5A-I**). Since the endogenous FAM161A
202 signal was too weak to quantify (**Figure 5G-I**), similar to results in mouse photoreceptors [18, 20], we
203 measured the signal length in the CC for only POC5 and Centrin (**Figure 5J**). The signal lengths of these
204 inner scaffold proteins at the CC were significantly shorter in cones than in rods, and these were
205 consistent with the CC lengths measured in Figure 3 (Rod POC5, 1383.09 ± 96.53 μm; Cone POC5,
206 911.01 ± 129.72 μm; Rod Centrin, 1449.83 ± 115.57 μm; Cone Centrin, 989.27 ± 172.09 μm; **Figure 5K**).
207 We then investigated the localization of several Y-link-associated proteins in canine photoreceptors.
208 The Y-link is a hallmark element of the transition zone in the primary cilium, exhibiting a distinctive Y-
209 shaped architecture that connects each microtubule doublet to the ciliary membrane [3]. In mammalian
210 photoreceptors, the CC is known as a region corresponding to the transition zone in the primary cilium,
211 and CEP290, a typical Y-link component protein, has been confirmed to localize outside each of the nine

212 tubulin axonemes in the CC of mouse photoreceptors [18]. As shown in Figure 2 and Supplementary
213 Figure 3, CEP290 localized at the CC in canine photoreceptors similar to its localization in mouse
214 photoreceptors. Here, we also found that the signal length of CEP290 at the CC is significantly shorter in
215 cones than in rods, consistent with the lengths of the CC shown in Figure 3 and Figure 5 (Rod CEP290,
216 1314.33 ± 118.71 μm; Cone CEP290, 891.09 ± 126.21 μm; **Figure 6A, B, C, and S**). Additionally, several
217 other Y-link-associated proteins, including RPGR, RPGRIP1 (LCA6), SPATA7 (LCA3), and NPHP5
218 (IQCB1), were found to have signal lengths comparable to CEP290 at the CC in both rods and cones
219 (**Figure 6D, E, G, H, J, K, M, N, and S**) and to localize outside the axoneme (**Figure 6F, I, L, O, and R**).
220 Finally, we found that MAP9, a microtubule-binding protein, localizes specifically to the CC in
221 photoreceptors (**Figure 6P and Q**). A homozygous variant in the MAP9 gene has been reported to
222 accelerate disease progression in a naturally-occurring canine *RPGRIP1*-associated cone-rod dystrophy
223 [33, 34]. The co-localization of MAP9 and RPGRIP1 in the CC of both photoreceptor subtypes suggests
224 a direct interaction between these proteins. Additionally, axial view images and quantification of signal
225 width at the CC revealed that MAP9 is located close to the tubulin axoneme, unlike the axial distribution
226 of other Y-link-associated proteins (**Figure 6R and T**). Mapping of these CC-specific proteins confirmed
227 a significant difference in the length of the CC between canine rods and cones.
228

229 **Molecular mapping of ciliary trafficking and distal appendage-related proteins on the basal bodies**
230 **in rod and cone PSC**

231 We next mapped the localization of proteins associated with the BB, the compartment on the basal
232 part of the tubulin-based PSC architecture. The intraflagellar transport (IFT) machinery is responsible for
233 anterograde and retrograde trafficking of ciliary proteins and consists of two multisubunit complexes, IFT-
234 A and IFT-B [35]. In mouse photoreceptors, it was demonstrated using immunoelectron microscopy that
235 several IFT particles have characteristic distribution around the BB and bulge region [8], and similar
236 localization of these particles has recently been confirmed using U-ExM as well [20, 21]. We confirmed
237 that in both canine rods and cones, IFT57, a component of the IFT-B complex [36], has a similar

238 distribution at the BB and bulge region as observed in mouse photoreceptors (**Figure 7A and B**).
239 Additionally, KIF3A, a component of kinesin-II, exhibited a similar distribution to the IFT particles in both
240 photoreceptor subtypes, albeit with a high level of background signal (**Supplementary Figure 5**). Axial
241 view images showed that IFT57 distributes along each of the nine tubulin axonemes at both the BB and
242 bulge region and is located closer to the axonemes at the bulge region than at the BB (**Figure 7C**). We
243 also found that the IFT57 signals at the BB were clearly divided into two layers (**Figure 7A and B**). The
244 distance from the proximal end of the BB to these signals was shorter in rods than in cones (**Figure 7D**),
245 consistent with the difference in BB length between the rods and cones presented in Figure 3.

246 Based on the characteristic distribution of IFT57 in the BB, we hypothesized that the IFT molecules
247 localize around distal appendages, also known as transition fibers, in the BB, as has been suggested in
248 previous publications [37, 38]. To verify this, we observed the distribution of CEP164 (NPHP15), a
249 representative distal appendage protein [39], in both rods and cones. As expected, CEP164 was localized
250 in the distal part of the BB in both rods and cones (**Figure 7E and F**), and the axial view exhibited a
251 broader radial distribution (**Figure 7G**), similar to that observed in recent studies using super-resolution
252 microscopy techniques [40, 41]. The distance from the BB proximal end to CEP164 signals was shorter
253 in rods than in cones, and these distances were comparable to these of the IFT57 signals at the distal
254 BB (**Figure 7D and M**).

255 Additionally, we found that SDCCAG8 (NPHP10), a retinal ciliopathy-associated protein [42, 43],
256 exhibits specific localization to the end of both BB and DC in rods and cones (**Figure 7H and I**). The axial
257 view images at the BB showed that SDCCAG8 has a nine-fold symmetry distribution outside the axoneme,
258 similar to IFT57 and CEP164 (**Figure 7J**). Moreover, co-immunostaining of SDCCAG8 with glutamylation
259 and γ-tubulin demonstrated that the SDCCAG8 signal on the ciliary axoneme is located between the BB
260 and CC (**Figure 7K and L**). The distance from the BB proximal end to SDCCAG8 was comparable to
261 that of CEP164 in both rods and cones (**Figure 7M**). Taken together, these results suggest that IFT57
262 and SDCCAG8 localize to distal appendages on the BB (**Figure 7N**). Furthermore, based on the distance
263 between distal and subdistal appendages suggested in previous study (~100 nm), the location of the

264 basal IFT57 signal in the BB is assumed to correspond to the location of the subdistal appendages [44].

265

266 **Molecular architecture of the ciliary rootlet in canine photoreceptors**

267 To address the peripheral structures of the PSC in canine photoreceptors, we mapped several
268 proteins related to the ciliary rootlet. Rootletin (CROCC) is a 220-kDa coiled coil protein identified as an
269 architectural component of the rootlet in mouse photoreceptors [45] and has been used as a marker of
270 ciliary rootlet in several studies [46, 47]. Consistent with previous reports, in canine retinas processed
271 with U-ExM, rootletin signals were observed as straight fibers in the photoreceptor IS, representing the
272 architecture of the ciliary rootlets (**Figure 8A**). In the magnified images, a rootlet stem extending straight
273 to the BB and a characteristic branch-like structure extending to the middle of the CC were observed in
274 the rod PSC (**Figure 8B and C, Supplementary Movie 1**). In contrast, cone photoreceptors exhibited a
275 curvilinear rootlet architecture that was quite different from that of rods. In cone photoreceptors, the base
276 of the rootlet did not contact the external limiting membrane, unlike in rods, and the ends of the rootlet
277 appeared to be directed toward the BB and DC, respectively (**Figure 8D and E, Supplementary Movie**
278 **2**). These structural features in cones were consistent among cone photoreceptor subtypes, S-cones and
279 L/M-cones (**Supplementary Figure 6**).

280 We found that ARL13B, a small GTPase belonging to the Arf-like Ras superfamily, is another protein
281 located in the ciliary rootlet of canine photoreceptors using the anti-human ARL13B antibody (17711-1-
282 AP). In studies of the primary cilium, ARL13B has frequently been employed as a marker for the ciliary
283 membrane [48, 49]. Since mutations in *ARL13B* gene have been associated with Joubert syndrome, a
284 systemic ciliopathy accompanied by retinal dystrophy, the localization of ARL13B in photoreceptors has
285 been discussed in various studies, with variable conclusions [50-53]. Although several recent reports
286 using mouse retina have claimed that endogenous ARL13B localizes to the photoreceptor OS
287 (**Supplementary Table 5**), we observed specific localization of ARL13B to the ciliary rootlet in U-ExM-
288 processed canine photoreceptors using the 17711-1-AP antibody (**Figure 8F**).

289 To ensure that this unique ARL13B localization was not an artifact of the U-ExM process, we

290 performed similar immunostaining on non-expanded cryosections. In non-expanded canine retina,
291 ARL13B localized primarily to the photoreceptor IS, consistent with the results in the U-ExM samples
292 (**Supplementary Figure 7A**). Moreover, we confirmed the specificity of this antibody by using the antigen
293 peptide, which completely blocked ARL13B labeling in the IS (**Supplementary Figure 7C**). Thus, the
294 rootlet-specific labeling with the 17711-1-AP antibody is unlikely to result from nonspecific binding. Similar
295 to rootletin, ARL13B labeled with 17711-1-AP exhibited straight localization in rods and curvilinear
296 localization in cones (**Figure 8G and H**). However, when we tested another anti-ARL13B antibody (clone
297 N295B/66), commonly used in mouse retina studies, we observed OS-specific localization of ARL13B,
298 consistent with previous reports, in both U-ExM and non-expanded samples (**Figure 8I, Supplementary**
299 **Figure 7B**). The fact that these two widely used anti-ARL13B antibodies exhibited completely different
300 labeling patterns in the canine retina underscores the need for further detailed studies on ARL13B
301 distribution in photoreceptors.
302
303 **Molecular architecture of the calyceal processes in canine photoreceptors**
304 Finally, we investigated the localization of protocadherin-15 (PCDH15), an Usher 1 protein, to
305 determine the presence or absence of calyceal processes in canine photoreceptors. Calyceal processes
306 are microvilli-like structures characterized by the localization of Usher proteins in the apical region of the
307 IS of human and nonhuman primate (NHP) photoreceptors and are absent in mouse photoreceptors [24].
308 Recent research on NHP photoreceptors using expansion microscopy has described the structural
309 organization of the calyceal processes based on the distribution of PCDH15 [17]. We followed this
310 approach on our canine retinal tissues. First, we determined that PCDH15 is located between the OS
311 and IS in both rods and cones in non-expanded retinal cryosections (**Figure 9A**). In the canine rod
312 photoreceptors processed by U-ExM, PCDH15 staining exhibited a characteristic C-shape, and its
313 distribution was limited to the base of the OS (**Figure 9B, Supplementary Movie 3**). In contrast, PCDH15
314 formed a microvilli-like structure surrounding the OS near the OS/IS junction in the canine cones (**Figure**
315 **9C, Supplementary Movie 4**). The distribution pattern of PCDH15 was identical between S-cones and

316 L/M-cones (**Figure 9D and E**). These differences of PCDH15 distribution between rods and cones were
317 consistent with the previous observations in NHP photoreceptors [17]. Additionally, we mapped Whirlin
318 (USH2D), an Usher 2 protein, which localized to the basal side of PCDH15, along with the CC tubulin
319 axoneme in both canine rods and cones. Whirlin exhibited a shorter distribution in cones compared to
320 rods correlating with the difference of CC length between these subtypes (**Figure 9F**). We also attempted
321 to localize another Usher 2 protein, VLGR1 (USH2C), in canine photoreceptors. However, identification
322 of specific VLGR1 signals using a commercially available primary antibody was unsuccessful.

323 Finally, we localized actin filaments by immunolabeling of β-actin. In non-expanded canine retina, β-
324 actin was distributed around the IS/OS interface in both cones and rods, although the signal intensity in
325 rods was lower than in cones (**Figure 10A**). However, in U-ExM samples, no actin filaments binding to
326 PCDH15 were observed in canine rods, whereas canine cones displayed distinct actin filaments linking
327 to the PCDH15-labeled microvilli-like architecture (**Figure 10B**). These findings were further supported
328 by Espin labeling, which indicated that calyceal processes-associated actin fibers in canine rods are more
329 fragile than in cones, making them unable to maintain their architecture after expansion (**Figure 10C and**
330 **D**). Taken together, these results suggest that in canine photoreceptors, while the localization of Usher
331 proteins at the IS/OS junction is present in both rods and cones, the microvilli-like distribution of Usher 1
332 protein is found only in cone photoreceptors, similar to what is observed in NHP photoreceptors.

Discussion

In the present study, we tested a U-ExM protocol to characterize the molecular architecture of the PSC using non-frozen and frozen archival canine retinal tissues. Utilizing archival samples, particularly from large animals such as dogs and NHP, presents significant advantages in terms of cost efficiency and biological resource management. This approach is not only economical but also allows for the maximization of previously collected biological materials. However, as highlighted in the publication reporting the original U-ExM protocol, the type and duration of fixation can influence the degree of tissue expansion [19]. Earlier studies applying U-ExM to the mouse retina typically used a short duration (15 minutes) of 4%PFA fixation [18, 21]. Here, we demonstrated that the duration of PFA fixation and long-term storage at -80°C do not significantly impact the degree of retinal tissue expansion, achieving approximately 4x isotropic expansion (**Figure 2**). This observation aligns with the recent reports that applied U-ExM to PFA-fixed frozen and formalin-fixed paraffin-embedded mouse tissues [20, 28]. Notably, our results showed that U-ExM enabled super-resolution imaging of archival samples that had been cryopreserved for over a decade, providing comparable imaging quality to that obtained from non-frozen samples. While some physical damage to the OS membrane architecture was observed in the frozen section-derived U-ExM samples compared to the non-frozen samples, the tubulin axoneme structure remained unaffected across the sample processing conditions. Additionally, longer durations of PFA fixation (≥ 24 hours), which are routinely used for cryopreservation of ocular tissues, proved beneficial in preserving the structure of the photoreceptor OS in U-ExM. These findings underscore the robustness of U-ExM for use with archival samples, facilitating ultrastructural observation in large animal tissues where non-frozen samples are often challenging to procure.

In the molecular mapping of the PSC in normal adult canine retinal tissue, we discovered that the tubulin-based PSC architecture differs significantly between the rods and cones (**Figure 3**). Specifically, cones exhibited longer BB and DC, shorter CC, and a longer and wider bulge region compared to rods. Additionally, the tubulin axonemes labeled by anti-AcTub were more prominent in the distal region of cones, which may suggest a more robust axoneme structure in cones than in rods. These structural

359 differences were corroborated by the distinct localization patterns of proteins within each PSC
360 compartment (**Figure 4-7**). While detailed comparisons of PSC molecular architecture between rods and
361 cones have been limited, our findings align with the known variations in the structural features of the OS
362 between these photoreceptor subtypes [54]. Previous studies have consistently reported that the CC
363 length in mature mouse rods ranges from approximately 1100 to 1500 nm [5, 18, 21], which is consistent
364 with the CC-specific protein signal lengths of approximately 1200 to 1400 nm observed in mature canine
365 rods in this study. Similarly, the DC length in mature mouse rods is approximately 300 nm [5], closely
366 matching the 270 nm measured in mature canine rods, indicating a conserved architecture of the CC and
367 BB in rods across these species. However, comparisons of cone PSC architecture between canine and
368 other vertebrates remain challenging due to a paucity of studies investigating the ultrastructure of cone
369 PSC to date. The significant architectural differences between rod and cone PSC observed in this study
370 underscore the necessity for further comprehensive investigations using retinal tissues from a variety of
371 vertebrate species. These investigations are crucial to determine whether the architectural distinctions in
372 the PSC between photoreceptor subtypes are unique to canine or represent a broader biological
373 phenomenon.

374 An interesting question raised by the observed architectural variation between rod and cone PSC is
375 its involvement in the differential pathological progression among photoreceptor subtypes. A notable
376 group of retinal ciliopathies, known as cone-rod dystrophy (CRD), is characterized by the progressive
377 degeneration of cones preceding that of the rods. In canine models of naturally-occurring retinal ciliopathy,
378 homozygous variants in genes such as *NPHP4*, *NPHP5*, and *RPGRIP1* have been identified as causes
379 of CRD [55-57], despite these genes being similarly expressed in both rods and cones. Previous studies
380 have suggested that these CRD-associated proteins are localized to the CC in photoreceptors [11, 58].
381 Our current study confirms that NPHP5 and RPGRIP1 are indeed localized outside the tubulin axoneme
382 at the CC in both photoreceptor subtypes (**Figure 6**). Given their comparable distribution, these proteins
383 are likely to have similar roles related to Y-links in both photoreceptor subtypes. Notably, the CC, where
384 the tubulin axoneme of the PSC is anchored to the plasma membrane by Y-links, is significantly shorter

385 in cones than in rods. This structural difference in the CC suggests that cones may be more susceptible
386 to mutations in Y-link-associated genes compared to rods. The relationship between the heterogeneity of
387 ciliopathy-associated phenotypes and the structural variations between rods and cones will be further
388 investigated in future studies, which will involve integrating respective retinal ciliopathy models with U-
389 ExM techniques to elucidate these differences.

390 Our study has also revealed significant differences in the architecture of the PSC rootlet between
391 rods and cones (**Figure 8**). Using U-ExM, we observed a linear shape of the rootlet in canine rods, which
392 is consistent with the morphology of the rootlet in mouse rods, as previously described in transmission
393 electron photomicrographs [10]. A new finding in this study is the identification of a rootlet branch
394 extending from the basal part of the PSC to the middle of the CC in rods. This branching structure has
395 also been observed in recent transmission electron photomicrographs of canine photoreceptors, where
396 it appears to be positioned on the opposite side of the PSC axoneme across the ciliary pocket [59],
397 although its functional role remains unclear. Another interesting discovery is the unique elliptical shape
398 of the cone rootlet. A recent study in NHP cones suggests that the cone rootlet has a markedly different
399 shape from the commonly recognized form in rod rootlet, although detailed morphological descriptions
400 have been lacking [17]. Here, we have demonstrated a curvilinear rootlet architecture in canine cones
401 using U-ExM. Additionally, unlike the rod rootlet, which extends towards the external limiting membrane,
402 the cone rootlet is entirely contained within the photoreceptor IS. Both rootlet structures likely play a
403 critical role in providing stable intracellular support for the PSC and their associated OS structures.
404 However, further studies are needed to elucidate the biological significance of these morphological
405 differences between rod and cone photoreceptors.

406 During the mapping of various cilia-associated proteins using U-ExM, we identified several proteins
407 with localization patterns that differed significantly from those reported in previous studies of the
408 vertebrate retina. Earlier studies, based on immunolabeling of non-expanded retinal samples, suggested
409 that CCDC66 localizes to the IS or OS [29-31]. However, given the properties of CCDC66 as a
410 microtubule-binding protein and previous findings from cell line studies [32], its localization to the OS or

411 IS in photoreceptors seems unlikely. Using U-ExM, we found that two anti-CCDC66 antibodies (PA5-
412 60642 and sc-102418) produced highly specific signals for the PSC axoneme, despite showing less
413 specificity in non-expanded retinal tissue (**Figure 4 and Supplementary Figure 4**). The PA5-46125
414 antibody, which did not detect signals in U-ExM, has a lower homology between its epitope and the
415 corresponding canine CCDC66 protein region compared to PA5-60642 (74% vs. 85%, respectively),
416 suggesting that this might affect its ability to accurately label the target protein. The improved specificity
417 of the other anti-CCDC66 antibodies (PA5-60642 and sc-102418) for the PSC axoneme could be
418 attributed to the enhanced accessibility of epitopes following the U-ExM procedure. On the other hand,
419 further investigation is required to explain the rootletin-specific signals obtained with the anti-human
420 ARL13B antibody (17711-1-AP). The labeling patterns of the two anti-ARL13B antibodies used in this
421 study were consistent between non-expanded and U-ExM samples, although the patterns differed
422 between the antibodies (**Figure 8 and Supplementary Figure 7**). A recent study using ARL13B-mCherry
423 Centrin2-GFP double transgenic mice reported an IS-specific and rootlet-like ARL13B-mCherry
424 distribution, which closely mirrors our findings in the canine retina, albeit restricted to the first 14 days
425 after birth [60]. Moreover, given that ARL13B-mcherry was widely detected from the OS to IS of mature
426 retina in the same transgenic mice, it is challenging to completely dismiss the rootlet-specific labeling of
427 the 17711-1-AP antibody observed in this study.

428 Finally, the application of U-ExM provided novel insights into the architecture of calyceal processes
429 in canine photoreceptors (**Figure 9 and 10**). Our findings indicate that canine cones possess microvilli-
430 like structures characterized by the distribution of PCDH15 around the basal part of the OS and the
431 presence of associated actin filaments. In contrast, canine rods lack microvilli-like PCDH15 distribution,
432 despite the localization of PCDH15 at the IS/OS junction. These differences in PCDH15 distribution
433 between rods and cones are similar to those observed in photoreceptors of NHPs in a previous study
434 [17]. Interestingly, at the electron microscopy level, microvilli-like structures have been observed in NHP
435 rods, though in smaller numbers compared to cones [24]; however, recent studies have shown an
436 absence of microvilli-like PCDH15 distribution in these rods [17]. This might suggest that the distribution

437 of PCDH15 in rods does not align with the microvilli-like architecture considered as calyceal processes.
438 To conclusively determine the presence or absence of calyceal processes in canine rods, further detailed
439 morphological studies using electron microscopy are necessary. The localization of Usher proteins
440 (PCDH15 and Whirlin) as well as actin filament-related proteins in canine photoreceptors aligns with the
441 patterns reported in NHP photoreceptors, suggesting that a canine IRD model may provide valuable
442 insights into pathogenesis of Usher syndrome, for which effective pathological models are challenging to
443 develop in rodents.

444 In conclusion, our study highlights the effectiveness of super-resolution imaging using U-ExM to
445 characterize the molecular architecture of the canine PSC. By employing U-ExM, we have achieved
446 detailed molecular mapping of numerous retinal ciliopathy-related proteins and have identified significant
447 structural differences in the PSC between rods and cones in canine photoreceptors (**Figure 11**). These
448 insights gained from this study pave the way for a better understanding of the alterations in PSC
449 molecular architecture and the efficacy of AAV-based gene augmentation therapies in established canine
450 models of retinal ciliopathy, such as those with mutations in *RPGR* [61], *NPHP5* [56], *RPGRIP1* [57], and
451 *CCDC66* [31], using U-ExM.

452

453 ## Material and methods

454 ### Animals

455 Retinal tissues from normal adult dogs were used for this study (**Supplementary Table 1**). All dogs
456 were housed under identical conditions, including diet and ambient illumination with a 12-hour light/12-
457 hour dark cycle, at the Retinal Disease Studies Facility (RDSF) at the University of Pennsylvania. The
458 studies strictly adhered to the ARVO Statement for the Use of Animals in Ophthalmic and Vision Research
459 and were approved by the Institutional Animal Care and Use Committee of the University of Pennsylvania.
460

461 ### Tissue processing for long-term cryopreservation

462 The procedures for long-term cryopreservation of normal adult canine ocular tissues were performed
463 as described in previous publications [62, 63]. In brief, following enucleation of euthanized dogs, the
464 posterior eyecups of the globes were isolated and the vitreous was gently extracted ~ 1 hour after fixation
465 in 4% PFA in 0.1 M phosphate-buffered saline (PBS). Fixation of the posterior eye cups was pursued for
466 an additional 2 hours, followed by an additional 24-hour fixation in 2% PFA in 0.1 M PBS at 4°C.
467 Subsequently, the eyecups were dissected into four quadrants, and the tissues were sequentially
468 cryoprotected for 24 hours each in 15% and 30% sucrose solutions in 0.1 M PBS at 4°C. Following
469 cryopreservation, the dissected tissues were embedded in optimal cutting temperature (OCT) medium
470 within disposable molds. The molds were then placed in shallow metal cups containing methylbutane
471 and immersed in a bath of liquid nitrogen for rapid freezing. The frozen OCT blocks were stored at -80°C
472 until cryosectioning was conducted. All cryopreserved samples used in this study had been stored for
473 more than 12 years at -80°C (**Supplementary Table 1**).
474

475 ### Immunohistochemistry on non-expanded cryosectioned retinal tissues

476 The frozen OCT blocks were cryosectioned at a thickness 10 μm and stored at -20°C until further
477 processing. Detailed methodology for immunostaining of non-expanded canine retinal cryosection has
478 been described in a previous publication [34]. Frozen sections were dried at room temperature (RT) for

479 60 minutes and then incubated in Dulbecco's PBS (D-PBS) for 10 minutes to remove the OCT compound.
480 Antigen retrieval was performed by treating the sections with pepsin reagent for 1 minute, followed by
481 incubation with blocking buffer (4.5% cold fish gelatin, 0.1% sodium azide, 5% bovine serum albumin,
482 and 0.25% Triton X-100 in D-PBS) for 60 minutes at RT. Retinal sections were then incubated overnight
483 at 4°C with primary antibodies (**Supplementary Table 3**) diluted in blocking buffer. In the specificity
484 confirmation study of the anti-human ARL13B antibody (Cat. #17711-1-AP), 50 μg/mL of ARL13B fusion
485 protein (Cat. #Ag12015) was pre-incubated with the antibody at RT for 2 hours before being applied to
486 retinal tissue. After three washes with D-PBS containing 0.1% of tween20 (PBS-T), antigen-antibody
487 complexes were visualized with Alexa Fluor-conjugated secondary antibodies (**Supplementary Table 4**)
488 and counterstained using Hoechst 33342. Fluorescein-conjugated Wheat Germ Agglutinin (WGA) was
489 diluted 1:200 in D-PBS and treated for 15 minutes after secondary antibody incubation. The reagents
490 used for conventional immunostaining were listed in Supplementary Table 2.
491

492 **Ultrastructure Expansion Microscopy (U-ExM) on canine retina**

493 Based on a U-ExM protocol previously developed for mouse retina [18], we tested U-ExM on non-
494 frozen and frozen archival canine retinal tissues. A schematic overview, photographs of each step, and
495 reagents associated with the U-ExM protocol used in this study are summarized in Supplementary Figure
496 1 and 2 and in Supplementary Table 2.

497 <u>(a) U-ExM on non-frozen canine neuroretinas</u>

498 After enucleation, the anterior part of eyeball, including the cornea, lens, and vitreous, was gently
499 removed. The posterior eyecups were fixed in PFA solution for either short (4% PFA for 15 minutes) or
500 long (4% PFA for 3 hours followed by 2% PFA for 24 hours) durations, and then 5 mm punches were
501 taken from the eyecups using a disposable biopsy punch (**Supplementary Figure 2A**). Once isolated
502 from RPE-choroid-sclera complex (**Supplementary Figure 2B, 2C**), a 5 mm retinal punch was placed in
503 a 14-mm microwell of a 35-mm petri dish and then incubated overnight in 300 μL of 2% acrylamide (AA)
504 + 1.4% formaldehyde (FA) solution at 37°C.

505 After removing the AA/FA solution, 45 μL of monomer solution (MS) composed of 25 μL of sodium
506 acrylate (SA; stock solution at 38% [w/w] diluted with nuclease-free water), 12.5 μL of AA (40% solution),
507 2.5 μL of N,N′-methylenebisacrylamide (BIS; 2% solution), and 5 μL of 10× PBS was added to the
508 microwell. After 90 minutes of incubation at RT, the MS was removed and 90 μL of MS containing
509 ammonium persulfate (APS) and tetramethylethylenediamine (TEMED) at a final concentration of 0.5%
510 was dropped onto the tissue, followed by covering with a 12 mm circular cover glass (**Supplementary**
511 **Figure 2D**). Subsequently, the 35-mm petri dish containing the tissue and MS solution was placed on ice
512 for 45 minutes, followed by 60 minutes incubation at 37°C to allow gelation.

513 Next, 1 mL of denaturation buffer (200 mM Sodium Dodecyl Sulfate (SDS), 200 mM Sodium Chloride
514 (NaCl), 50 mM Tris Base in deionized distilled water (ddH_2O), pH 9) were added to the petri dish for 15
515 minutes at RT with gentle agitation. The gel was carefully detached from the microwell using a spatula
516 and then incubated in a 1.5 mL tube filled with denaturation buffer for 90 minutes at 95°C. Immediately
517 after the denaturation step, the gel was transferred to a beaker filled with ddH_2O, and the ddH_2O was
518 replaced twice, every 30 minutes, for the first-round of expansion.

519 The following day, after measuring the diameter with a ruler (**Supplementary Figure 2E**), the
520 expanded gel containing retinal tissue was sliced with a razor blade to obtain approximately 1-2 mm thick
521 cross sections. These sections were then placed in a well of 24-well plate filled with D-PBS containing
522 calcium & magnesium (D-PBS-$Ca^{2+}Mg^{2+}$) for the immunostaining steps.

523 <u>(b) U-ExM for cryosections from frozen retinal tissue</u>

524 Twenty-μm-thick cryosections were obtained from the frozen posterior cup tissues that had been
525 fixed with PFA using the longer protocol, cryoprotected in sucrose, and embedded in OCT media. The
526 frozen sections on a slide glass were thawed at RT for 10 minutes (**Supplementary Figure 2F**), and a
527 square was drawn around the tissue section using a hydrophobic marker (ImmEdge Pen). After drying
528 for 60 minutes at RT, 100 μL of D-PBS-$Ca^{2+}Mg^{2+}$ was added into the hydrophobic square for 10 minutes
529 to wash out the OCT compound.

530 After removal of D-PBS, the sections were reacted with the AA/FA solution overnight, followed by

531 penetration with MS for 90 minutes, as was done for non-frozen retinal punches. For each retinal section,
532 45 µL of MS containing APS and TEMED per section was dropped onto the tissue, and a 12 mm circular
533 cover glass was placed on the solution (**Supplementary Figure 2G**). After performing gelation,
534 denaturation, and the first-round expansion as done for non-frozen retinal punches, the diameter of the
535 gel was measured with a ruler (**Supplementary Figure 2H**). The gel containing the retinal tissue was
536 then cut into approximately 1 cm squares using a razor blade and then in a well of 24-well plate filled with
537 D-PBS-$Ca^{2+}Mg^{2+}$.

538 Immunohistochemistry for U-ExM samples

539 After 10 minutes of incubation of the gels in D-PBS, the solution in the well was replaced with 300
540 µL of blocking buffer containing the primary antibodies (**Supplementary Table 3**). The gels were
541 incubated with the primary antibody solution overnight at RT with gentle shaking, followed by 3 washes
542 with 1 mL of PBS-T for 5 minutes each. Alexa Fluor-conjugated secondary antibodies (**Supplementary**
543 **Table 4**) were diluted in the blocking buffer at a concentration of 1/500 and incubated with the gel for 2
544 hours at RT, protected from light. Next, 100 µL of Hoechst 33342 solution, diluted 1/1000 in D-PBS, was
545 added to the wells and gently shaken for 30 minutes, followed by 3 washes with 1 mL of PBS-T. After the
546 washes, each gel was transferred using a spatula to a well of a 6-well plate filled with 10 mL ddH_2O and
547 incubated for 30 minutes to achieve the second-round expansion. The ddH_2O was replaced twice, every
548 30 minutes. The gels were then stored in ddH_2O at 4°C, protected from light, until confocal imaging.

549

550 **Confocal imaging**

551 Prior to imaging, 14-mm microwells of 35-mm petri dishes were filled with 0.1 mg/mL poly-D-lysine
552 and kept at RT for 1 hour for coating to prevent drifting of the gels. After removing the poly-D-lysine
553 solution, the microwells were washed three times with ddH_2O, dried, and then stored at 4°C.

554 Image acquisition was performed on the Leica Stellaris 8 FALCON confocal FLIM microscope using
555 a 63× (1.20 NA) water objective. The lateral and axial views were obtained by orienting the expanded gel
556 on the bottom of the microwell to face either the retinal cross-section or photoreceptor outer segment

557 downward. Z-stacks for the lateral view were acquired with 0.2 μm z-intervals, an x, y pixel size of 45.09
558 nm, and an imaging speed of 400 Hz. Representative images of the lateral view are shown as maximum
559 projection images unless specified. Sigle images of the axial view were obtained with an x, y pixel size
560 of 22.55 nm and an imaging speed of 100 Hz. The images were processed using Leica Application Suite
561 X (LAS X) software for deconvolution with LIGHTNING function, as well as for building merged and
562 maximum projection images, and 3D rendering.
563
564 **Quantification**
565 Gel diameter
566 The gel diameter after the first-round expansion was measured using a ruler and then divided by the
567 gel diameter before expansion (1.2 mm) to calculate the degree of gel expansion.
568 Expansion factor
569 The expansion factor was calculated by dividing the width of the AcTub-labeled axoneme on the CC
570 of U-ExM samples by the previously reported CC diameter of non-expanded mice photoreceptors (200.84
571 nm), quantified using cryo-electron tomography [5]. A total of 40 photoreceptors in all U-ExM conditions
572 were subjected to measurement of AcTub signal width using LAS X software manually. The width of the
573 CC was consistent across all U-ExM conditions, and the expansion factor in this study was determined
574 to be 3.83 by averaging the values of all U-ExM conditions. This expansion factor was used for every
575 quantification.
576 Protein signal length, width, and distance from the proximal end of the BB
577 Lengths, widths, and distance of protein signals were measured using the “Draw scalebar” function
578 in LAS X software manually to fit the photoreceptor curvature. AcTub-labeled axoneme spread was
579 measured at four different locations of the rod and cone photoreceptors corresponding to the CC or bulge
580 region: +1000, +500, 0, and -500 nm. The distal end of the glutamylation signal located outside the tubulin
581 axoneme was used to define the 0 location. Each measurement was subsequently corrected using the
582 expansion factor.

583

584 **Statistical analysis**

585 Comparisons between 2 groups were performed using the nonparametric Mann-Whitney U test.
586 Comparisons among more than 3 groups were conducted using the nonparametric Kruskal-Wallis test
587 with Dunn's multiple-comparison test. Every measurement was performed on at least 2 individual eyes.
588 Quantitative data are represented as scatter dot plots, with the center line and error bars in the graphs
589 indicating the mean and standard deviation (± SD), respectively. The significance level is denoted as
590 follows: nonsignificant (n.s.) $P > 0.05$, *$P < 0.05$, **$P < 0.01$, ***$P < 0.001$, ****$P < 0.0001$. All statistical
591 analyses were performed using GraphPad Prism 10. The data underlying the graphs shown in all the
592 figures are included in Supplementary Data.

593

594 **Data availability**

595 All data are available in the main text or the supplementary information.

596

Author Contributions

K.T. and W.A.B. participated in the conception, experimental design, and interpretation of the data for this work. K.T. was responsible for the acquisition and analysis of data, statistical analysis, and the drafting of the manuscript. R.S. and W.A.B. reviewed and edited the manuscript. All authors reviewed the manuscript, approved its submission, and take full responsibility for the manuscript.

Acknowledgements

We express our gratitude to Qin Liu and Eric A. Pierce of Harvard Medical School for providing the RP1 antibody [64]; Penn Vet Imaging Core Facility (Research Resource Identifier: SCR_022764) for technical support; the staff of the Division of Experimental Retinal Therapies for their excellent support; and the staff of RDSF at University of Pennsylvania for their outstanding animal care. This study was supported by NIH grants R01EY006855, R01EY017549, R01EY033049, P30EY001583, S10OD032305-01A1, and Foundation Fighting Blindness.

Conflict of interest

The authors declare that the research was conducted in the absence of any commercial or financial relationships that could be construed as a potential conflict of interest.

615 **References**

616 1. Lamb TD, Collin SP, Pugh EN, Jr. Evolution of the vertebrate eye: opsins, photoreceptors, retina
617 and eye cup. Nat Rev Neurosci. 2007;8(12):960-76. doi: 10.1038/nrn2283.

618 2. Park K, Leroux MR. Composition, organization and mechanisms of the transition zone, a gate for
619 the cilium. EMBO Rep. 2022;23(12):e55420. Epub 20221121. doi: 10.15252/embr.202255420.

620 3. Mercey O, Mukherjee S, Guichard P, Hamel V. The molecular architecture of the ciliary transition
621 zones. Curr Opin Cell Biol. 2024;88:102361. Epub 20240421. doi: 10.1016/j.ceb.2024.102361.

622 4. Barnes CL, Malhotra H, Calvert PD. Compartmentalization of Photoreceptor Sensory Cilia. Front
623 Cell Dev Biol. 2021;9:636737. Epub 20210204. doi: 10.3389/fcell.2021.636737.

624 5. Gilliam JC, Chang JT, Sandoval IM, Zhang Y, Li T, Pittler SJ, et al. Three-dimensional architecture
625 of the rod sensory cilium and its disruption in retinal neurodegeneration. Cell. 2012;151(5):1029-41. doi:
626 10.1016/j.cell.2012.10.038.

627 6. Rachel RA, Yamamoto EA, Dewanjee MK, May-Simera HL, Sergeev YV, Hackett AN, et al.
628 CEP290 alleles in mice disrupt tissue-specific cilia biogenesis and recapitulate features of syndromic
629 ciliopathies. Hum Mol Genet. 2015;24(13):3775-91. Epub 20150409. doi: 10.1093/hmg/ddv123.

630 7. Pulvermüller A, Giessl A, Heck M, Wottrich R, Schmitt A, Ernst OP, et al. Calcium-dependent
631 assembly of centrin-G-protein complex in photoreceptor cells. Mol Cell Biol. 2002;22(7):2194-203. doi:
632 10.1128/mcb.22.7.2194-2203.2002.

633 8. Sedmak T, Wolfrum U. Intraflagellar transport molecules in ciliary and nonciliary cells of the retina.
634 J Cell Biol. 2010;189(1):171-86. doi: 10.1083/jcb.200911095.

635 9. Sánchez-Bellver L, Toulis V, Marfany G. On the Wrong Track: Alterations of Ciliary Transport in
636 Inherited Retinal Dystrophies. Front Cell Dev Biol. 2021;9:623734. Epub 20210305. doi:
637 10.3389/fcell.2021.623734.

638 10. Wensel TG, Potter VL, Moye A, Zhang Z, Robichaux MA. Structure and dynamics of
639 photoreceptor sensory cilia. Pflugers Arch. 2021;473(9):1517-37. Epub 20210528. doi: 10.1007/s00424-
640 021-02564-9.

641 11. Potter VL, Moye AR, Robichaux MA, Wensel TG. Super-resolution microscopy reveals
642 photoreceptor-specific subciliary location and function of ciliopathy-associated protein CEP290. JCI
643 Insight. 2021;6(20). Epub 20211022. doi: 10.1172/jci.insight.145256.
644 12. Haggerty KN, Eshelman SC, Sexton LA, Frimpong E, Rogers LM, Agosto MA, et al. Super-
645 resolution mapping in rod photoreceptors identifies rhodopsin trafficking through the inner segment
646 plasma membrane as an essential subcellular pathway. PLoS Biol. 2024;22(1):e3002467. Epub
647 20240108. doi: 10.1371/journal.pbio.3002467.
648 13. Robichaux MA, Potter VL, Zhang Z, He F, Liu J, Schmid MF, et al. Defining the layers of a sensory
649 cilium with STORM and cryoelectron nanoscopy. Proc Natl Acad Sci U S A. 2019;116(47):23562-72. Epub
650 20191105. doi: 10.1073/pnas.1902003116.
651 14. Chen F, Tillberg PW, Boyden ES. Optical imaging. Expansion microscopy. Science.
652 2015;347(6221):543-8. Epub 20150115. doi: 10.1126/science.1260088.
653 15. Hümpfer N, Thielhorn R, Ewers H. Expanding boundaries - a cell biologist's guide to expansion
654 microscopy. J Cell Sci. 2024;137(7). Epub 20240417. doi: 10.1242/jcs.260765.
655 16. Moye AR, Robichaux MA, Wensel T. Expansion Microscopy of Mouse Photoreceptor Cilia. Adv
656 Exp Med Biol. 2023;1415:395-402. doi: 10.1007/978-3-031-27681-1_58.
657 17. Verschueren A, Boucherit L, Ferrari U, Fouquet S, Nouvel-Jaillard C, Paques M, et al. Planar
658 polarity in primate cone photoreceptors: a potential role in Stiles Crawford effect phototropism. Commun
659 Biol. 2022;5(1):89. Epub 20220124. doi: 10.1038/s42003-021-02998-y.
660 18. Mercey O, Kostic C, Bertiaux E, Giroud A, Sadian Y, Gaboriau DCA, et al. The connecting cilium
661 inner scaffold provides a structural foundation that protects against retinal degeneration. PLoS Biol.
662 2022;20(6):e3001649. Epub 20220616. doi: 10.1371/journal.pbio.3001649.
663 19. Gambarotto D, Zwettler FU, Le Guennec M, Schmidt-Cernohorska M, Fortun D, Borgers S, et al.
664 Imaging cellular ultrastructures using expansion microscopy (U-ExM). Nat Methods. 2019;16(1):71-4.
665 Epub 20181217. doi: 10.1038/s41592-018-0238-1.
666 20. Arsenijevic Y, Chang N, Mercey O, El Fersioui Y, Koskiniemi-Kuendig H, Joubert C, et al. Fine-

667 tuning FAM161A gene augmentation therapy to restore retinal function. EMBO Mol Med. 2024;16(4):805-
668 22. Epub 20240319. doi: 10.1038/s44321-024-00053-x.
669 21. Faber S, Mercey O, Junger K, Garanto A, May-Simera H, Ueffing M, et al. Gene augmentation of
670 LCA5-associated Leber congenital amaurosis ameliorates bulge region defects of the photoreceptor
671 ciliary axoneme. JCI Insight. 2023;8(10). Epub 20230522. doi: 10.1172/jci.insight.169162.
672 22. Slijkerman RW, Song F, Astuti GD, Huynen MA, van Wijk E, Stieger K, et al. The pros and cons
673 of vertebrate animal models for functional and therapeutic research on inherited retinal dystrophies. Prog
674 Retin Eye Res. 2015;48:137-59. Epub 20150501. doi: 10.1016/j.preteyeres.2015.04.004.
675 23. Kostic C, Arsenijevic Y. Animal modelling for inherited central vision loss. J Pathol.
676 2016;238(2):300-10. Epub 20151113. doi: 10.1002/path.4641.
677 24. Sahly I, Dufour E, Schietroma C, Michel V, Bahloul A, Perfettini I, et al. Localization of Usher 1
678 proteins to the photoreceptor calyceal processes, which are absent from mice. J Cell Biol.
679 2012;199(2):381-99. Epub 20121008. doi: 10.1083/jcb.201202012.
680 25. Beltran WA, Cideciyan AV, Guziewicz KE, Iwabe S, Swider M, Scott EM, et al. Canine retina has
681 a primate fovea-like bouquet of cone photoreceptors which is affected by inherited macular degenerations.
682 PLoS One. 2014;9(3):e90390. Epub 20140305. doi: 10.1371/journal.pone.0090390.
683 26. Winkler PA, Occelli LM, Petersen-Jones SM. Large Animal Models of Inherited Retinal
684 Degenerations: A Review. Cells. 2020;9(4). Epub 20200403. doi: 10.3390/cells9040882.
685 27. Uzbekov RE, Maurel DB, Aveline PC, Pallu S, Benhamou CL, Rochefort GY. Centrosome fine
686 ultrastructure of the osteocyte mechanosensitive primary cilium. Microsc Microanal. 2012;18(6):1430-41.
687 Epub 20121121. doi: 10.1017/s1431927612013281.
688 28. Langner E, Puapatanakul P, Pudlowski R, Alsabbagh DY, Miner JH, Horani A, et al. Ultrastructure
689 expansion microscopy (U-ExM) of mouse and human kidneys for analysis of subcellular structures.
690 Cytoskeleton (Hoboken). 2024. Epub 20240507. doi: 10.1002/cm.21870.
691 29. Dekomien G, Vollrath C, Petrasch-Parwez E, Boevé MH, Akkad DA, Gerding WM, et al.
692 Progressive retinal atrophy in Schapendoes dogs: mutation of the newly identified CCDC66 gene.

693 Neurogenetics. 2010;11(2):163-74. Epub 20090924. doi: 10.1007/s10048-009-0223-z.
694 30. Gerding WM, Schreiber S, Schulte-Middelmann T, de Castro Marques A, Atorf J, Akkad DA, et al.
695 Ccdc66 null mutation causes retinal degeneration and dysfunction. Hum Mol Genet. 2011;20(18):3620-
696 31. Epub 20110616. doi: 10.1093/hmg/ddr282.
697 31. Murgiano L, Becker D, Spector C, Carlin K, Santana E, Niggel JK, et al. CCDC66 frameshift
698 variant associated with a new form of early-onset progressive retinal atrophy in Portuguese Water Dogs.
699 Sci Rep. 2020;10(1):21162. Epub 20201203. doi: 10.1038/s41598-020-77980-5.
700 32. Odabasi E, Conkar D, Deretic J, Batman U, Frikstad KM, Patzke S, et al. CCDC66 regulates
701 primary cilium length and signaling via interactions with transition zone and axonemal proteins. J Cell Sci.
702 2023;136(3). Epub 20230202. doi: 10.1242/jcs.260327.
703 33. Forman OP, Hitti RJ, Boursnell M, Miyadera K, Sargan D, Mellersh C. Canine genome assembly
704 correction facilitates identification of a MAP9 deletion as a potential age of onset modifier for RPGRIP1-
705 associated canine retinal degeneration. Mamm Genome. 2016;27(5-6):237-45. Epub 20160326. doi:
706 10.1007/s00335-016-9627-x.
707 34. Takahashi K, Kwok JC, Sato Y, Aguirre GD, Miyadera K. Molecular characterization of MAP9 in
708 the photoreceptor sensory cilia as a modifier in canine RPGRIP1-associated cone-rod dystrophy. Front
709 Cell Neurosci. 2023;17:1226603. Epub 20230815. doi: 10.3389/fncel.2023.1226603.
710 35. Ishikawa H, Marshall WF. Intraflagellar Transport and Ciliary Dynamics. Cold Spring Harb
711 Perspect Biol. 2017;9(3). Epub 20170301. doi: 10.1101/cshperspect.a021998.
712 36. Bhogaraju S, Engel BD, Lorentzen E. Intraflagellar transport complex structure and cargo
713 interactions. Cilia. 2013;2(1):10. Epub 20130814. doi: 10.1186/2046-2530-2-10.
714 37. Yang TT, Chong WM, Wang WJ, Mazo G, Tanos B, Chen Z, et al. Super-resolution architecture
715 of mammalian centriole distal appendages reveals distinct blade and matrix functional components. Nat
716 Commun. 2018;9(1):2023. Epub 20180522. doi: 10.1038/s41467-018-04469-1.
717 38. Hazime KS, Zhou Z, Joachimiak E, Bulgakova NA, Wloga D, Malicki JJ. STORM imaging reveals
718 the spatial arrangement of transition zone components and IFT particles at the ciliary base in

719 Tetrahymena. Sci Rep. 2021;11(1):7899. Epub 20210412. doi: 10.1038/s41598-021-86909-5.
720 39. Graser S, Stierhof YD, Lavoie SB, Gassner OS, Lamla S, Le Clech M, et al. Cep164, a novel
721 centriole appendage protein required for primary cilium formation. J Cell Biol. 2007;179(2):321-30. doi:
722 10.1083/jcb.200707181.
723 40. Katoh Y, Chiba S, Nakayama K. Practical method for superresolution imaging of primary cilia and
724 centrioles by expansion microscopy using an amplibody for fluorescence signal amplification. Mol Biol
725 Cell. 2020;31(20):2195-206. Epub 20200729. doi: 10.1091/mbc.E20-04-0250.
726 41. Bowler M, Kong D, Sun S, Nanjundappa R, Evans L, Farmer V, et al. High-resolution
727 characterization of centriole distal appendage morphology and dynamics by correlative STORM and
728 electron microscopy. Nat Commun. 2019;10(1):993. Epub 20190301. doi: 10.1038/s41467-018-08216-4.
729 42. Otto EA, Hurd TW, Airik R, Chaki M, Zhou W, Stoetzel C, et al. Candidate exome capture identifies
730 mutation of SDCCAG8 as the cause of a retinal-renal ciliopathy. Nat Genet. 2010;42(10):840-50. Epub
731 20100912. doi: 10.1038/ng.662.
732 43. Tsutsumi R, Chaya T, Tsujii T, Furukawa T. The carboxyl-terminal region of SDCCAG8 comprises
733 a functional module essential for cilia formation as well as organ development and homeostasis. J Biol
734 Chem. 2022;298(3):101686. Epub 20220204. doi: 10.1016/j.jbc.2022.101686.
735 44. Chong WM, Wang WJ, Lo CH, Chiu TY, Chang TJ, Liu YP, et al. Super-resolution microscopy
736 reveals coupling between mammalian centriole subdistal appendages and distal appendages. Elife.
737 2020;9. Epub 20200403. doi: 10.7554/eLife.53580.
738 45. Yang J, Liu X, Yue G, Adamian M, Bulgakov O, Li T. Rootletin, a novel coiled-coil protein, is a
739 structural component of the ciliary rootlet. J Cell Biol. 2002;159(3):431-40. Epub 20021111. doi:
740 10.1083/jcb.200207153.
741 46. Ryu S, Ko D, Shin B, Rhee K. The intercentriolar fibers function as docking sites of centriolar
742 satellites for cilia assembly. J Cell Biol. 2024;223(4). Epub 20240228. doi: 10.1083/jcb.202105065.
743 47. Yang J, Gao J, Adamian M, Wen XH, Pawlyk B, Zhang L, et al. The ciliary rootlet maintains long-
744 term stability of sensory cilia. Mol Cell Biol. 2005;25(10):4129-37. doi: 10.1128/mcb.25.10.4129-

745 4137.2005.
746 48. Hua K, Ferland RJ. Fixation methods can differentially affect ciliary protein immunolabeling. Cilia.
747 2017;6:5. Epub 20170324. doi: 10.1186/s13630-017-0045-9.
748 49. Gigante ED, Taylor MR, Ivanova AA, Kahn RA, Caspary T. ARL13B regulates Sonic hedgehog
749 signaling from outside primary cilia. Elife. 2020;9. Epub 20200304. doi: 10.7554/eLife.50434.
750 50. Cantagrel V, Silhavy JL, Bielas SL, Swistun D, Marsh SE, Bertrand JY, et al. Mutations in the cilia
751 gene ARL13B lead to the classical form of Joubert syndrome. Am J Hum Genet. 2008;83(2):170-9. doi:
752 10.1016/j.ajhg.2008.06.023.
753 51. Kim YK, Kim JH, Yu YS, Ko HW, Kim JH. Localization of primary cilia in mouse retina. Acta
754 Histochem. 2013;115(8):789-94. Epub 20130419. doi: 10.1016/j.acthis.2013.03.005.
755 52. Dilan TL, Moye AR, Salido EM, Saravanan T, Kolandaivelu S, Goldberg AFX, et al. ARL13B, a
756 Joubert Syndrome-Associated Protein, Is Critical for Retinogenesis and Elaboration of Mouse
757 Photoreceptor Outer Segments. J Neurosci. 2019;39(8):1347-64. Epub 20181220. doi:
758 10.1523/jneurosci.1761-18.2018.
759 53. Hanke-Gogokhia C, Wu Z, Sharif A, Yazigi H, Frederick JM, Baehr W. The guanine nucleotide
760 exchange factor Arf-like protein 13b is essential for assembly of the mouse photoreceptor transition zone
761 and outer segment. J Biol Chem. 2017;292(52):21442-56. Epub 20171031. doi:
762 10.1074/jbc.RA117.000141.
763 54. Mustafi D, Engel AH, Palczewski K. Structure of cone photoreceptors. Prog Retin Eye Res.
764 2009;28(4):289-302. Epub 20090606. doi: 10.1016/j.preteyeres.2009.05.003.
765 55. Wiik AC, Wade C, Biagi T, Ropstad EO, Bjerkås E, Lindblad-Toh K, et al. A deletion in
766 nephronophthisis 4 (NPHP4) is associated with recessive cone-rod dystrophy in standard wire-haired
767 dachshund. Genome Res. 2008;18(9):1415-21. Epub 20080807. doi: 10.1101/gr.074302.107.
768 56. Goldstein O, Mezey JG, Schweitzer PA, Boyko AR, Gao C, Bustamante CD, et al. IQCB1 and
769 PDE6B mutations cause similar early onset retinal degenerations in two closely related terrier dog breeds.
770 Invest Ophthalmol Vis Sci. 2013;54(10):7005-19. Epub 20131025. doi: 10.1167/iovs.13-12915.

771 57. Mellersh CS, Boursnell ME, Pettitt L, Ryder EJ, Holmes NG, Grafham D, et al. Canine RPGRIP1
772 mutation establishes cone-rod dystrophy in miniature longhaired dachshunds as a homologue of human
773 Leber congenital amaurosis. Genomics. 2006;88(3):293-301. Epub 20060627. doi:
774 10.1016/j.ygeno.2006.05.004.
775 58. Patil H, Tserentsoodol N, Saha A, Hao Y, Webb M, Ferreira PA. Selective loss of RPGRIP1-
776 dependent ciliary targeting of NPHP4, RPGR and SDCCAG8 underlies the degeneration of photoreceptor
777 neurons. Cell Death Dis. 2012;3(7):e355. Epub 20120719. doi: 10.1038/cddis.2012.96.
778 59. Ripolles-Garcia A, Murgiano L, Ziolkowska N, Marinho FP, Roszak K, Iffrig S, et al. Natural
779 disease history of a canine model of oligogenic RPGRIP1-cone-rod dystrophy establishes variable effects
780 of previously and newly mapped modifier loci. Hum Mol Genet. 2023;32(13):2139-51. doi:
781 10.1093/hmg/ddad046.
782 60. Ning K, Sendayen BE, Kowal TJ, Wang B, Jones BW, Hu Y, et al. Primary Cilia in Amacrine Cells
783 in Retinal Development. Invest Ophthalmol Vis Sci. 2021;62(9):15. doi: 10.1167/iovs.62.9.15.
784 61. Zhang Q, Acland GM, Wu WX, Johnson JL, Pearce-Kelling S, Tulloch B, et al. Different RPGR
785 exon ORF15 mutations in Canids provide insights into photoreceptor cell degeneration. Hum Mol Genet.
786 2002;11(9):993-1003. doi: 10.1093/hmg/11.9.993.
787 62. Takahashi K, Beltran WA, Sudharsan R. An optimized workflow for transcriptomic analysis from
788 archival paraformaldehyde-fixed retinal tissues collected by laser capture microdissection. Exp Eye Res.
789 2024;246:109989. Epub 20240703. doi: 10.1016/j.exer.2024.109989.
790 63. Aguirre GD, Cideciyan AV, Dufour VL, Ripolles-García A, Sudharsan R, Swider M, et al. Gene
791 therapy reforms photoreceptor structure and restores vision in NPHP5-associated Leber congenital
792 amaurosis. Mol Ther. 2021;29(8):2456-68. Epub 20210327. doi: 10.1016/j.ymthe.2021.03.021.
793 64. Liu Q, Zhou J, Daiger SP, Farber DB, Heckenlively JR, Smith JE, et al. Identification and
794 subcellular localization of the RP1 protein in human and mouse photoreceptors. Invest Ophthalmol Vis
795 Sci. 2002;43(1):22-32.
796

797 ## Figure legends

798 **Figure 1. Schematic diagram of the rod photoreceptor sensory cilium**

799 Overall view of the architecture of the rod photoreceptor (left) and detailed depiction of each compartment
800 in the PSC (right). The PSC tubulin axoneme originates from the BB located in the IS and extends through
801 the CC to reach the OS. Just beyond the CC, the axoneme expands at the bulge region and then tapers
802 toward the distal part of the OS. Abbreviations: BB, basal body; CC, connecting cilium; DC, daughter
803 centriole; IS, inner segment; ONL, outer nuclear layer; OS, outer segment; PSC, photoreceptor sensory
804 cilium.

805

806 **Figure 2. Comparison of tissue integrity and protein localization under different U-ExM conditions**
807 **(A-D)** Low-magnification images of the outer retina stained for rhodopsin (yellow), cone arrestin (CAR;
808 cyan), and α-tubulin (magenta) in U-ExM samples subjected to different preservation/fixation protocols
809 (non-frozen/short-fix, A; non-frozen/long-fix, B; frozen/long-fix, C) and non-expanded samples (D). (D) is
810 enlarged 3.8 times more than (A-C). Scale bars: 5 μm, without correction for expansion factor. **(E)**
811 Widefield view of a U-ExM sample stained for α-tubulin (yellow) and acetylated α-tubulin (AcTub;
812 magenta). Scale bar: 5 μm, without correction for expansion factor. **(F-I)** Details of α-tubulin (yellow) and
813 AcTub (magenta) staining in the canine PSC under U-ExM (F-H) and non-expanded (I) conditions. (I) is
814 enlarged 3.8 times more than (F-H). The lower panels show axial view at the CC for each U-ExM condition,
815 indicated by white arrowheads. Scale bars: lateral view = 500 nm; axial view = 200 nm, without correction
816 for expansion factor. **(J, K)** Widths of AcTub-labeled CC (J) and BB proximal end (K) under different U-
817 ExM conditions. Sample size: n = 40 photoreceptors. For each condition, 4 individual punches or
818 cryosections from 2-4 eyes were stained. Non-significant (n.s., $P > 0.05$) as assessed by Kruskal-Wallis
819 test with Dunn's multiple-comparison test. **(L-S)** Molecular localization of Centrin (cyan, L-O) and CEP290
820 (green, P-S) in normal canine PSC under U-ExM with different preservation/fixation protocols (non-
821 frozen/short-fix, L, P; non-frozen/long-fix, M, Q; frozen/long-fix, N, R) and non-expanded (O, S) conditions.
822 (O, S) are enlarged 3.8 times more than (L-N, P-R). Scale bars: lateral view = 500 nm; axial view = 200

823 nm, without correction for expansion factor. Abbreviations: BB, basal body; CC, connecting cilium; DC,
824 daughter centriole; INL, inner nuclear layer; IS, inner segment; ONL, outer nuclear layer; OS, outer
825 segment; PFA, paraformaldehyde; PSC, photoreceptor sensory cilium.
826
827 **Figure 3. Tubulin-based molecular structure of rod and cone PSC in normal adult canine**
828 **photoreceptors**
829 **(A-D)** Confocal images of expanded adult canine PSC stained for AcTub (magenta) and glutamylated
830 microtubules (white). Rod and cone photoreceptors were identified by labeling with rhodopsin (yellow, A)
831 and cone arrestin (CAR; cyan, C), respectively. Black, red, and white arrowheads on bulge region, CC,
832 and BB correspond to the respective axial views in (B, D). Scale bars: lateral view = 500 nm; axial view
833 = 200 nm, after correction for expansion factor. **(E)** Schematic diagram showing the measurement of
834 length and width in the CC, BB, and DC. The tubulin axoneme labeled with AcTub and the glutamylation
835 signals on Y-links are represented in magenta and grey, respectively. **(F-I)** Comparison of length and
836 width on the BB (F, G) and the CC (H, I) between rod and cone PSC. **(J, K)** Rod (J) and cone (K) PSC
837 illustrating the measurements of AcTub-labeled axoneme width at four locations relative to the bulge
838 region: +1000, +500, 0, and -500 nm. The distal end of the glutamylation signal located outside of the
839 tubulin axoneme was used to define the 0 nm location. Scale bars: 500 nm, after correction for expansion
840 factor. **(L, M)** Measurements of tubulin width in rod (L) and cone (M) PSC at the four locations illustrated
841 in (J, K). **(N)** Comparison of tubulin width between rod and cone photoreceptors at the four locations
842 shown in (J, K). Sample size: n = 12-22 from ≥ 2 individual eyes. *P < 0.05, **P < 0.01, ***P < 0.001, and
843 ****P < 0.0001 as assessed by Kruskal-Wallis test with Dunn's multiple-comparison test (F, G) or Mann–
844 Whitney test (H, I, L-N). Abbreviations: BB, basal body; CC, connecting cilium; DC, daughter centriole;
845 PSC, photoreceptor sensory cilium.
846
847 **Figure 4. Molecular architecture of the bulge region and distal axoneme in normal canine rod and**
848 **cone PSC**

849 **(A-F)** Lateral views of expanded adult canine PSC stained for LCA5 (orange, A, B), RP1 (green, C, D),
850 and CCDC66 (white, E, F) in rod (A, C, E) and cone (B, D, F) photoreceptors, respectively. CCDC66 is
851 labeled using an antibody provided by Invitrogen (Cat. #PA5-60642). Scale bars: 500 nm, after correction
852 for expansion factor. **(G-L)** Co-immunolabeling with LCA5/RP1 (orange/green, G-I) and RP1/CCDC66
853 (green/white, J-L) in each photoreceptor subtype. The right panels (I, L) show axial views of the bulge
854 region indicated by the white arrowheads in each staining. The white dashed lines represent the starting
855 position of each protein signal on the tubulin axoneme. Scale bars: lateral view = 500 nm; axial view =
856 200 nm, after correction for expansion factor. **(M)** Comparison of distance from the proximal end of the
857 BB to the starting point of each protein signal between rod and cone PSC. Sample size: n = 12-24 from
858 ≥ 3 individual eyes. ***P < 0.001, and ****P < 0.0001 as assessed by Mann–Whitney test. **(N)** Model
859 illustrating the differences in molecular architecture of the distal part of the PSC, including the bulge
860 region, between rod and cone photoreceptors. Abbreviations: BB, basal body; PSC, photoreceptor
861 sensory cilium.
862
863 **Figure 5. Location of inner scaffold proteins in normal canine rod and cone PSC**
864 **(A-I)** Confocal images of expanded adult canine PSC stained for POC5 (green, A-C), Centrin (green, D-
865 F), and FAM161A (green, G-H). Rod and cone photoreceptors were identified by labeling with rhodopsin
866 (yellow, A, D, G) and CAR (cyan, B, E, H), respectively. The right panels (C, F, I) show axial views of the
867 CC for each protein, indicated by white arrowheads. Scale bars: lateral view = 500 nm; axial view = 200
868 nm, after correction for expansion factor. **(J)** Schematic diagram illustrating the measurement of signal
869 length in the CC. The tubulin axoneme labeled with AcTub and inner scaffold proteins are represented in
870 magenta and green, respectively. **(K)** Comparison of POC5 and Centrin signal lengths between rod and
871 cone PSC. Sample size: n = 9-18 from ≥ 2 individual eyes. ****P < 0.0001 as assessed by Mann–Whitney
872 test. Abbreviations: CC, connecting cilium; PSC, photoreceptor sensory cilium.
873
874 **Figure 6. Molecular mapping of multiple connecting cilium-related proteins in normal canine rod**

875 **and cone PSC**

876 **(A-R)** Expanded normal canine PSC stained for CEP290 (green, A-C), RPGR (green, D-F), RPGRIP1
877 (green, G-I), SPATA7 (green, J-L), NPHP5 (green, M-O), and MAP9 (white, P-R) in rod (A, D, G, J, M, P)
878 and cone (B, E, H, K, N, Q) photoreceptors, respectively. Axial views of the CC for each protein, indicated
879 by white arrowheads, are shown in (C, F, I, L, O, R). Scale bars: lateral view = 500 nm; axial view = 200
880 nm, after correction for expansion factor. **(S)** Measurement of signal length of each protein on the CC in
881 rod and cone PSC. Sample size: n = 11-26 from ≥ 3 individual eyes. **(T)** Comparison of signal width
882 between CEP290, MAP9, and AcTub in rod and cone PSC. Sample size: n = 11-35 from ≥ 3 individual
883 eyes. *P < 0.05 and ****P < 0.0001 as assessed by Mann–Whitney test (S) or Kruskal-Wallis test with
884 Dunn's multiple-comparison test (T). Abbreviations: CC, connecting cilium; PSC, photoreceptor sensory
885 cilium.

886

887 **Figure 7. Localization of ciliary trafficking and distal appendage-related proteins in normal canine**
888 **rod and cone PSC**

889 **(A-C)** Confocal U-ExM images of normal canine PSC stained for AcTub (magenta) and IFT57 (green) in
890 rod (A) and cone (B) photoreceptors, respectively. Insets, which are enlarged single z-scan images from
891 (A) and (B), highlight the detailed localization of IFT57 around the BB. Black, red, and white arrowheads
892 on bulge region, CC, and BB correspond to the axial views shown in (C). Scale bars: lateral view = 500
893 nm; axial view = 200 nm, after correction for expansion factor. **(D)** Comparison of distance from the
894 proximal end of the BB to IFT57 signals around the basal part of PSC between rod and cone PSC.
895 Sample size: n = 12-20 from ≥ 3 individual eyes. **(E-J)** Expanded normal canine photoreceptors labeled
896 for distal appendage-marker (CEP164; green, E-G) and SDCCAG8 (green, H-J) in rod (E, H) and cone
897 (F, I) photoreceptors, respectively. Axial views of the basal part of PSC for each protein, indicated by
898 white arrowheads, are shown in (G, J). Scale bars: lateral view = 500 nm; axial view = 200 nm, after
899 correction for expansion factor. **(K-L)** Co-immunolabeling with glutamylation/SDCCAG8 (white/green, K)
900 and γ-tubulin/SDCCAG8 (orange/green, L). Scale bars: 500 nm, after correction for expansion factor. **(M)**

901 Measurement of distance from the proximal end of the BB to the signal of each protein in rod and cone
902 PSC. Sample size: n = 13-26 from ≥ 3 individual eyes. **P < 0.01, ***P < 0.001, and ****P < 0.0001 as
903 assessed by Mann–Whitney test. **(N)** Model illustrating the identified location of IFT57 and SDCCAG8
904 around the distal appendages in normal canine photoreceptors. Abbreviations: BB, basal body; CC,
905 connecting cilium; DC, daughter centriole; PSC, photoreceptor sensory cilium.
906
907 **Figure 8. Structural characterization of the ciliary rootlet in normal canine rod and cone**
908 **photoreceptors**
909 **(A)** Widefield view of a U-ExM sample stained for rootletin (green) and AcTub (magenta). Scale bar: 1
910 μm, after correction for expansion factor. **(B-E)** High-magnification of expanded normal canine PSC
911 stained for rootletin (green) and AcTub (magenta) in rod (B, C) and cone (D, E) photoreceptors,
912 respectively. 3D rendering images were shown in (C, E) from different angles. Scale bars: 2D maximum
913 projection = 1 μm; 3D view = 500 nm, after correction for expansion factor. **(F)** Co-immunolabeling with
914 anti-human ARL13B [Cat. #17711-1-AP]/anti-human rootletin (white/green) in a U-ExM sample of normal
915 canine retina. Scale bars: 1 μm, after correction for expansion factor. **(G-I)** Confocal images of expanded
916 adult canine photoreceptors labeled with anti-human ARL13B [Cat. #17711-1-AP]/anti-AcTub
917 (white/magenta, G, H) and anti-mouse ARL13B [clone N295B/66]/anti-AcTub (white/magenta, I). Rod
918 and cone photoreceptors were identified by labeling with rhodopsin (yellow, G, I) and CAR (cyan, H),
919 respectively. Scale bars: low-magnification view = 1 μm; high-magnification view = 500 nm, after
920 correction for expansion factor. Abbreviations: CC, connecting cilium; IS, inner segment; ONL, outer
921 nuclear layer; PSC, photoreceptor sensory cilium.
922
923 **Figure 9. Molecular architecture of calyceal processes in normal canine photoreceptors**
924 **(A)** Widefield view of a non-expanded retinal cryosection stained for wheat germ agglutinin (WGA;
925 orange), and protocadherin 15 (PCDH15; green). The right panels show details of PCDH15 location in
926 rod and cone photoreceptors. Scale bar: 5 μm, without correction for expansion factor. **(B-E)** Confocal

927 images of expanded adult canine photoreceptors stained for PCDH15 (green) and AcTub (magenta). Rod
928 and cone photoreceptors were identified by labeling with rhodopsin (yellow, B), CAR (cyan, C), blue-
929 opsin (blue, D), and red/green-opsin (red, E) respectively. The right panels in (B, C) and (E, D) are
930 showing 3D rendering images of one photoreceptor. Scale bars: 500 nm, after correction for expansion
931 factor. Abbreviations: IS, inner segment; ONL, outer nuclear layer; OS, outer segment.
932
933 **Figure 10. Actin filaments associated with calyceal processes**
934 **(A, C)** Co-labeling with β-actin/WGA (orange/cyan, A) and Espin/WGA (orange/cyan, C) in non-expanded
935 canine retinal tissues. The right panels show details of actin filaments location associated with calyceal
936 processes in rod and cone photoreceptors. Scale bar: 5 μm, without correction for expansion factor. **(B,**
937 **E)** Co-labeling with β-actin/PCDH15 (orange/green, B) and Espin/PCDH15 (orange/green, D) in U-ExM
938 samples of normal canine retina. Abbreviations: IS, inner segment; ONL, outer nuclear layer; OS, outer
939 segment. Scale bars: 500 nm, after correction for expansion factor.
940
941 **Figure 11. Schematic summary diagrams of the molecular architecture of PSC and calyceal**
942 **processes, and the distribution of retinal ciliopathy-associated proteins in normal canine rod and**
943 **cone photoreceptors**
944 **(A)** Overview of the architecture of normal canine rod (left) and cone (right) photoreceptors. **(B)**
945 Comparison of PSC molecular architecture between rod and cone photoreceptors. Cone PSC has a
946 longer and wider bulge region, a longer BB, a longer DC, and a shorter CC than those of rod PSC. **(C)**
947 Structural differences of PSC rootlet between rod and cone photoreceptors. Rod photoreceptors have a
948 straight rootlet extending toward the ONL, whereas the rootlet of cones forms a curvilinear shape. **(D)**
949 Distribution of calyceal processes-related proteins in rod and cone photoreceptors. In rod photoreceptors,
950 the localization of PCDH15 is limited to the IS/OS junction, while in cone photoreceptors, PCDH15 shows
951 a microvilli-like distribution accompanied by actin filaments. Abbreviations: BB, basal body; CC,
952 connecting cilium; DC, daughter centriole; IS, inner segment; ONL, outer nuclear layer; OS, outer

953 segment; PSC, photoreceptor sensory cilium.

954

955 **Supplementary Figure 1. Overview of the modified U-ExM protocol for non-frozen and frozen-**
956 **archival canine retinal tissues**

957 AA, acrylamide; ASP, ammonium persulfate; ddH_2O, distilled deionized water; FA, formaldehyde; MS,
958 monomer solution; OCT, optimal cutting temperature; PFA, paraformaldehyde; RT, room temperature;
959 TEMED, tetramethylethylenediamine.

960

961 **Supplementary Figure 2. Tissue processing and gel expansion in U-ExM with canine retinal**
962 **tissues**

963 **(A)** Collection of 5 mm tissue punches from PFA fixed- non-frozen canine posterior eyecup using a
964 disposable biopsy punch. **(B, C)** Isolation of retinal tissue from the 5 mm tissue complex (B, before; C,
965 after isolation). **(D)** Gelation of the 5 mm retinal punch using a 12 mm circular cover glass. **(E)** First-round
966 expansion of the gel including the non-frozen retinal punch. **(F)** Twenty-µm-thick canine retinal
967 cryosection. **(G)** Gelation of the canine retinal cryosection using a 12 mm circular cover glass. **(H)** First-
968 round expansion of the gel including the retinal section. **(I)** Comparison of gel diameter after the first-
969 round expansion between different fixation conditions. Sample size: n = 4 individual punches or
970 cryosections from 2-4 eyes per fixation/storage condition. Non-significant (n.s., $P > 0.05$) by Kruskal-
971 Wallis test with Dunn's multiple-comparison test.

972

973 **Supplementary Figure 3. Co-immunolabeling of CEP290 and glutamination on the connecting**
974 **cilium of normal canine photoreceptors**

975 Confocal images of expanded adult canine PSC stained for AcTub (magenta), glutamination (white), and
976 CEP290 (green). The lower panels show axial views of the CC, indicated by white arrowheads. Scale
977 bars: lateral view = 500 nm; axial view = 200 nm, after correction for expansion factor. Abbreviations: CC,
978 connecting cilium.

979

980 **Supplementary Figure 4. Evaluation of the reactivity of multiple anti-CCDC66 antibodies in canine**
981 **retinal tissues**

982 **(A, C, E)** Confocal images of non-expanded retinal cryosections stained for rhodopsin (yellow), CCDC66
983 (white), and AcTub (magenta). Panels (A), (C), and (E) show the results of IHC using three different anti-
984 human CCDC66 antibodies: PA5-60642, PA5-46125, and sc-102418, respectively. Scale bars: 5 μm,
985 without correction for expansion factor. **(B, D, F)** Expanded normal canine PSC labeled with the PA5-
986 60642 antibody (white, B), PA5-46125 antibody (white, D), and sc-102418 antibody (white, F). The PSC
987 axoneme is visualized by AcTub labeling (magenta). Scale bars: 500 nm, after correction for expansion
988 factor. Abbreviations: CC, connecting cilium; IS, inner segment; OS, outer segment, PSC, photoreceptor
989 sensory cilium.

990

991 **Supplementary Figure 5. Localization of KIF3A in normal canine rod and cone PSC**

992 **(A, B)** Confocal U-ExM images of normal canine PSC stained for AcTub (magenta) and KIF3A (green) in
993 rod (A) and cone (B) photoreceptors, respectively. KIF3A signal shows a similar localization pattern to
994 IFT57 around the BB and bulge region. Abbreviations: BB, basal body; PSC, photoreceptor sensory
995 cilium.

996

997 **Supplementary Figure 6. Stricture of the PSC rootlet in normal canine blue and red/green cone**
998 **photoreceptors**

999 **(A, B)** 3D rendering images of U-ExM samples stained for rootletin (green) with blue-opsin (blue, A) or
1000 red/green-opsin (red, B). No significant differences are observed in the architecture of the PSC rootlet
1001 among the different cone subtypes. Scale bars: 500 nm, after correction for expansion factor.
1002 Abbreviation: PSC, photoreceptor sensory cilium.

1003

1004 **Supplementary Figure 7. Immunostaining for ARL13B on non-expanded normal canine retinal**

1005 **cryosection**

1006 **(A, B)** Widefield (left) and high-magnification (right) view of a non-expanded retinal cryosection stained
1007 for rhodopsin (yellow), ARL13B (white), and AcTub (magenta). (A) and (B) show the results of IHC using
1008 anti-human ARL13B antibody (17711-1-AP) and ant-mouse ARL13B antibody (clone N295B/66),
1009 respectively. Consistent with the findings in U-ExM samples, ARL13B labeled with the 17711-1-AP
1010 antibody predominantly localized to the IS, whereas the N295B/66 antibody exhibits OS-specific signals
1011 in the non-expanded cryosection. **(C)** Specificity confirmation experiment for the 17711-1-AP antibody.
1012 The blocking peptide for the 17711-1-AP antibody completely inhibited its reaction in the IS. Scale bars:
1013 5 μm. Abbreviations: INL, inner nuclear layer; IS, inner segment; ONL, outer nuclear layer; OS, outer
1014 segment.

1015

Figure 1

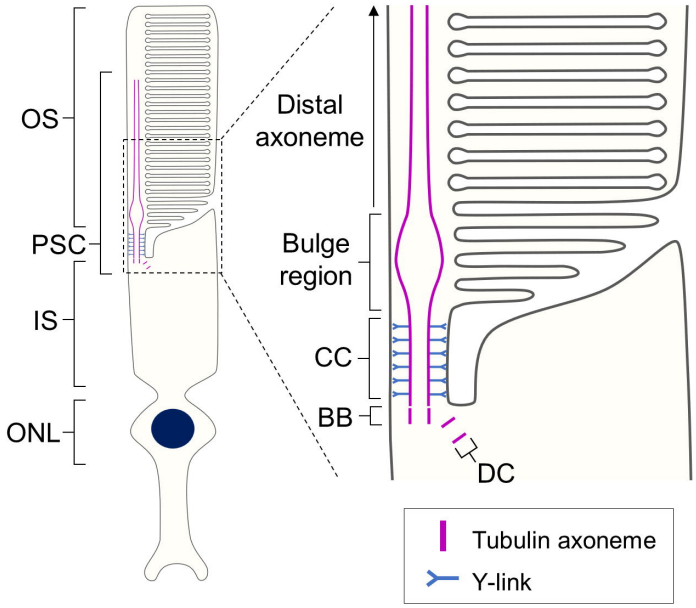
OS
PSC
IS
ONL
Distal
axoneme
Bulge
region
CC
BB
DC
Tubulin axoneme
Y-link

Figure 2

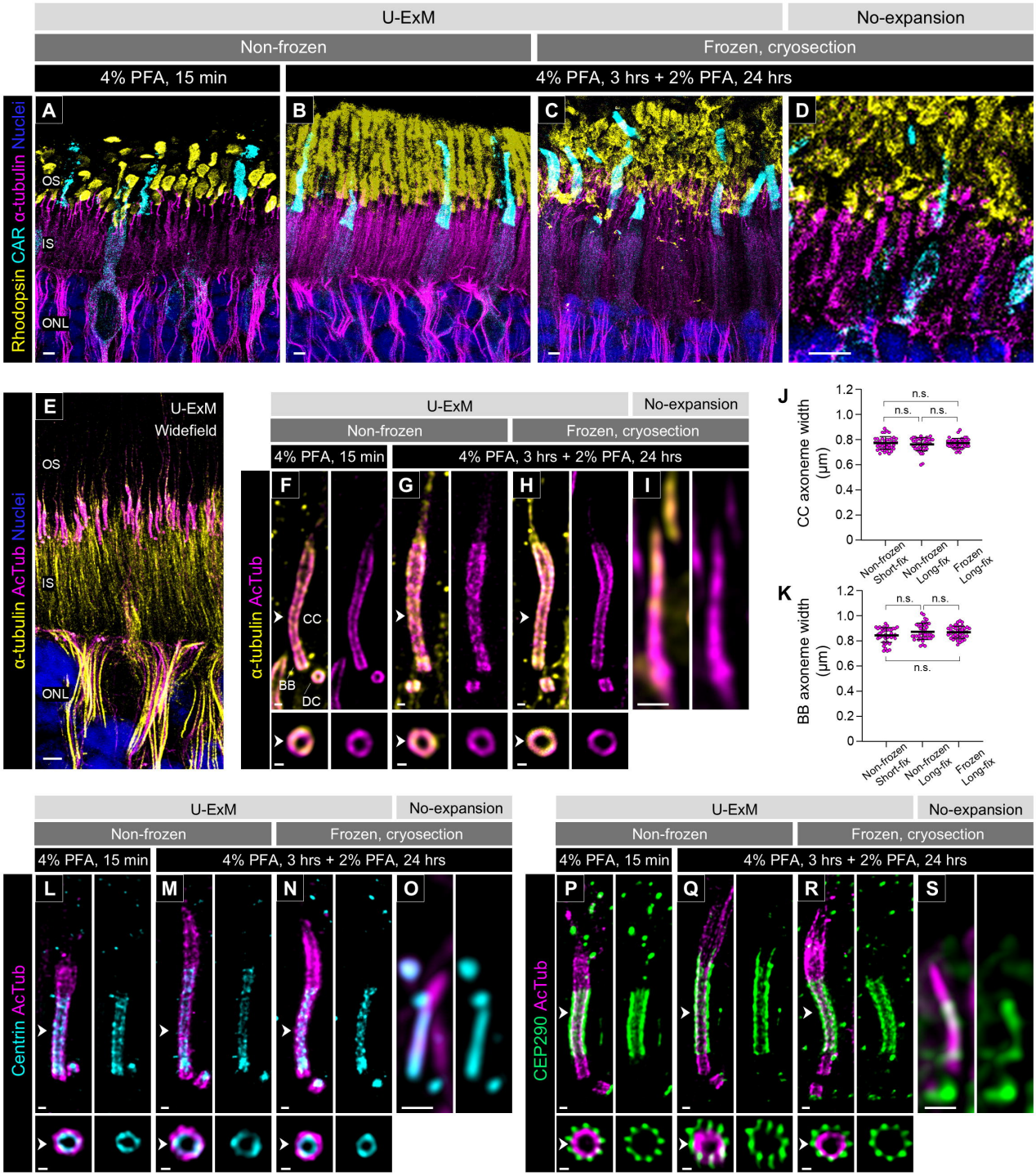
U-ExM
No-expansion
Non-frozen
Frozen, cryosection
4% PFA, 15 min
4% PFA, 3 hrs + 2% PFA, 24 hrs
Rhodopsin CAR α-tubulin Nuclei
A
B
C
D
OS
IS
ONL
E
U-ExM
Widefield
α-tubulin AcTub Nuclei
F
G
H
I
CC
BB
DC
α-tubulin AcTub
J
CC axoneme width (µm)
n.s.
Non-frozen Short-fix
Non-frozen Long-fix
Frozen Long-fix
K
BB axoneme width (µm)
L
M
N
O
Centrin AcTub
P
Q
R
S
CEP290 AcTub

Figure 3

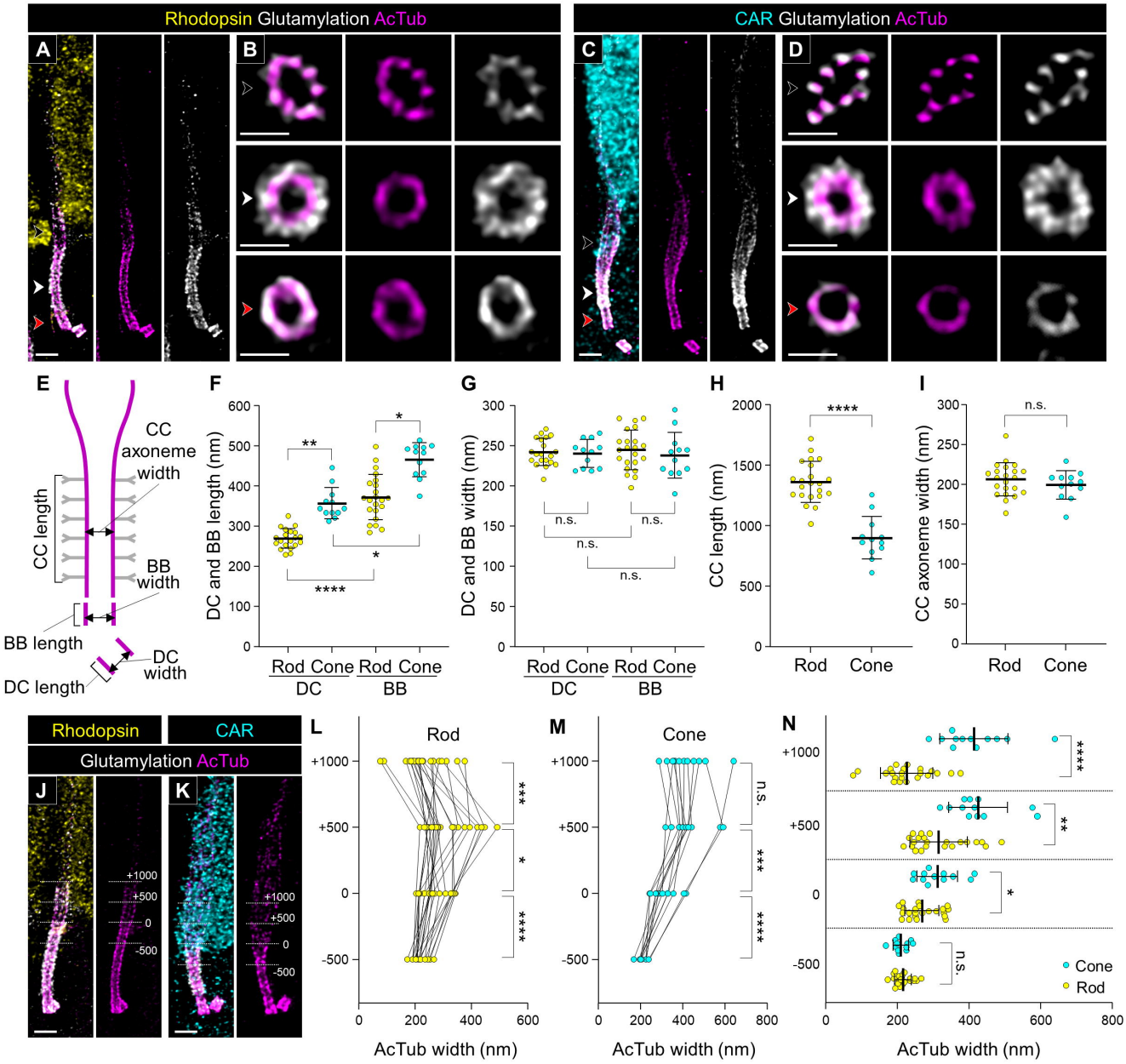
Rhodopsin Glutamylation AcTub
CAR Glutamylation AcTub
A
B
C
D
E
CC axoneme width
CC length
BB width
BB length
DC width
DC length
F
DC and BB length (nm)
Rod Cone Rod Cone
DC BB
G
DC and BB width (nm)
n.s.
H
CC length (nm)
Rod Cone
I
CC axoneme width (nm)
n.s.
Rhodopsin CAR
Glutamylation AcTub
J
K
L
Rod
M
Cone
N
AcTub width (nm)
Cone
Rod

Figure 4

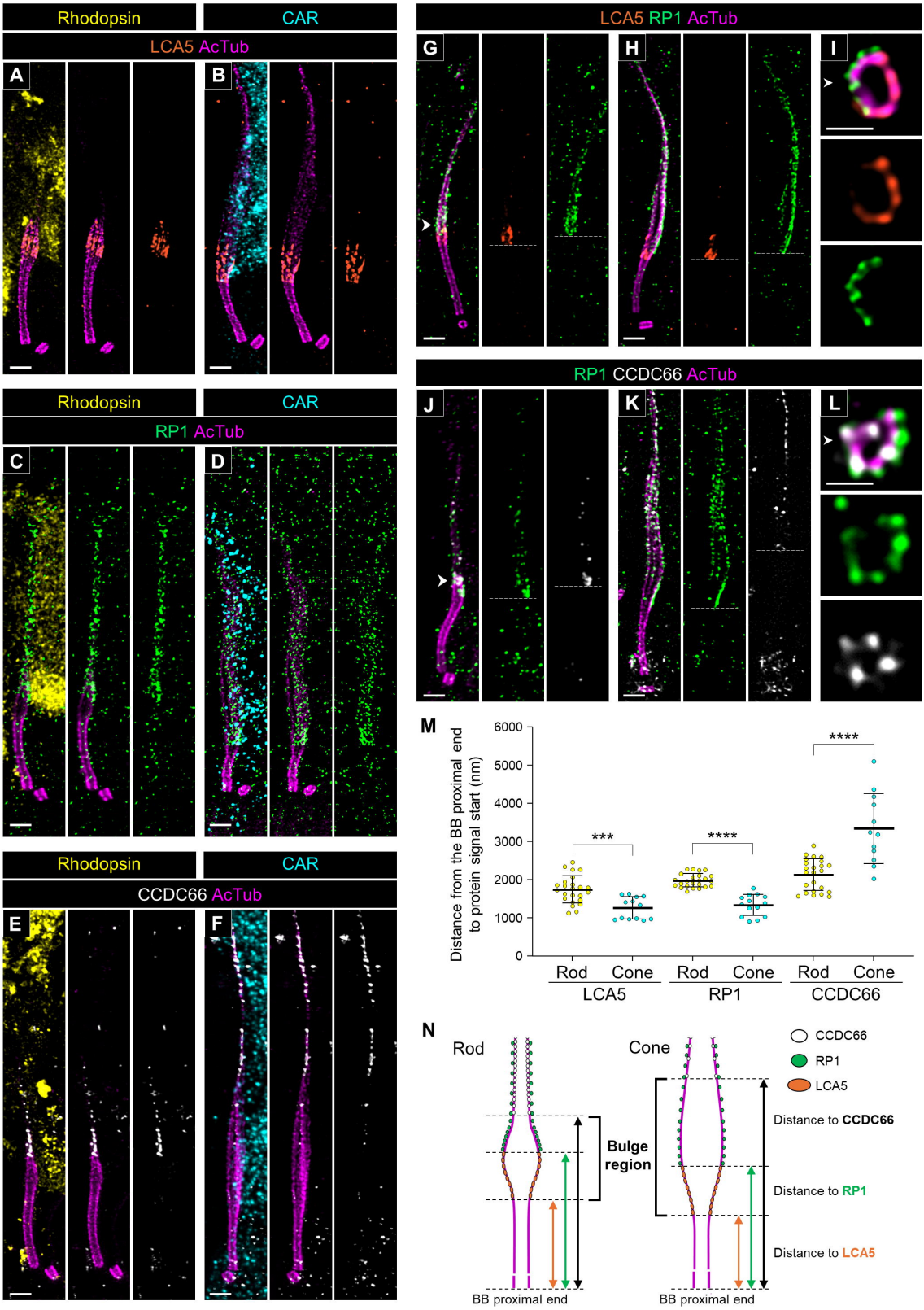
Rhodopsin
CAR
LCA5 AcTub
A
B
Rhodopsin
CAR
RP1 AcTub
C
D
Rhodopsin
CAR
CCDC66 AcTub
E
F
LCA5 RP1 AcTub
G
H
I
RP1 CCDC66 AcTub
J
K
L
M
Distance from the BB proximal end to protein signal start (nm)
6000
5000
4000
3000
2000
1000
0
***
****
****
Rod
Cone
Rod
Cone
Rod
Cone
LCA5
RP1
CCDC66
N
Rod
Cone
CCDC66
RP1
LCA5
Bulge region
Distance to CCDC66
Distance to RP1
Distance to LCA5
BB proximal end
BB proximal end

Figure 5

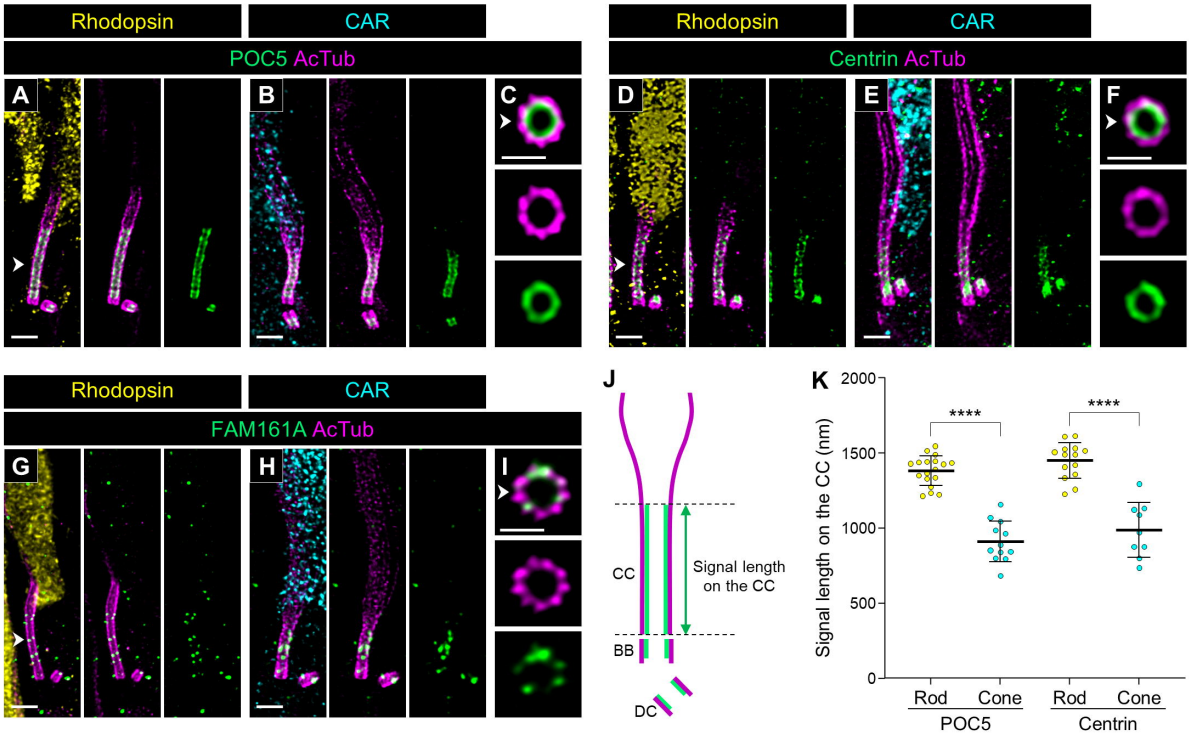
Rhodopsin
CAR
POC5 AcTub
A
B
C
Rhodopsin
CAR
Centrin AcTub
D
E
F
Rhodopsin
CAR
FAM161A AcTub
G
H
I
J
CC
Signal length on the CC
BB
DC
K
Signal length on the CC (nm)
2000
1500
1000
500
0
****
****
Rod
Cone
Rod
Cone
POC5
Centrin

Figure 6

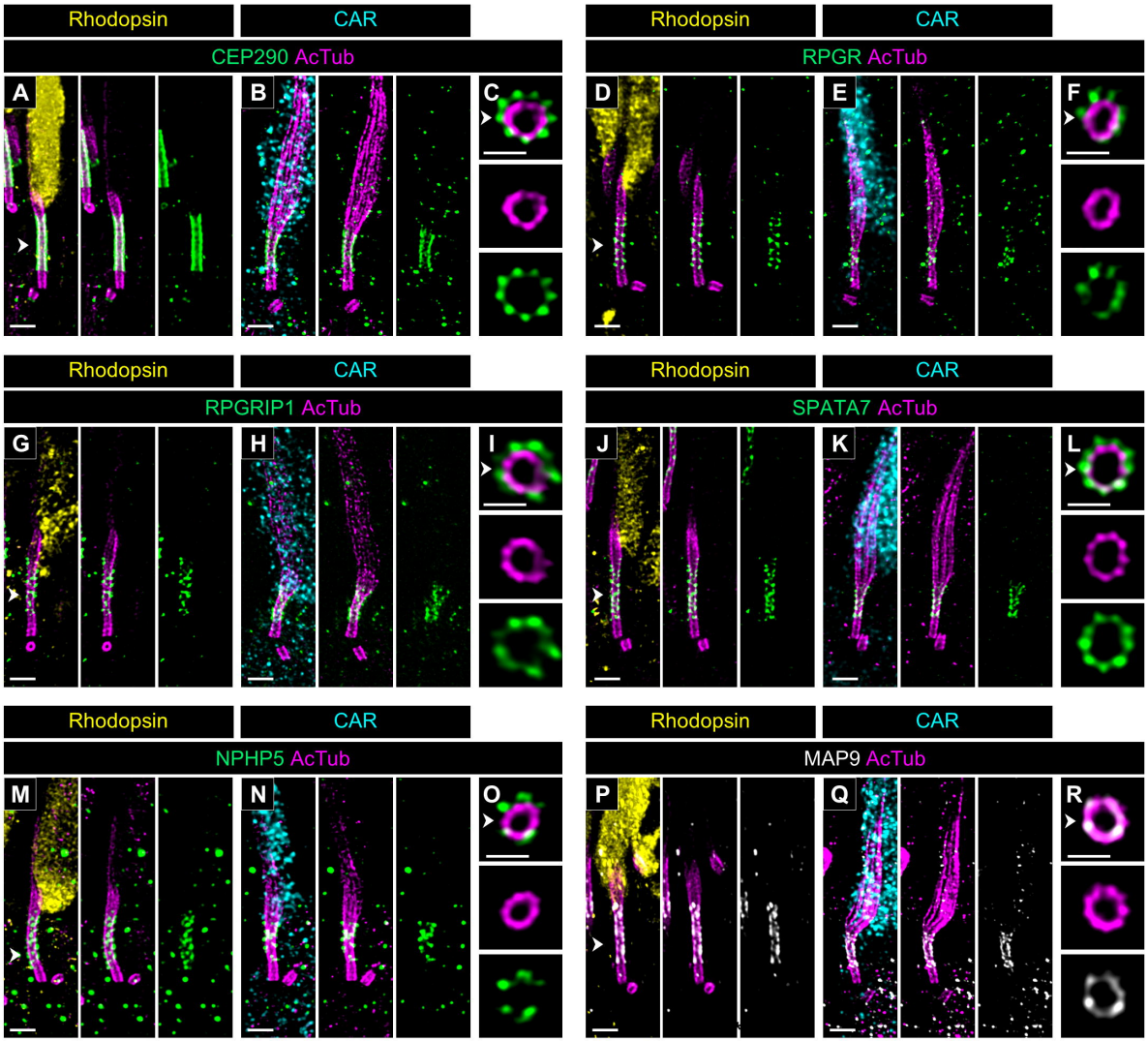
Rhodopsin
CAR
CEP290 AcTub
RPGR AcTub
RPGRIP1 AcTub
SPATA7 AcTub
NPHP5 AcTub
MAP9 AcTub
A
B
C
D
E
F
G
H
I
J
K
L
M
N
O
P
Q
R

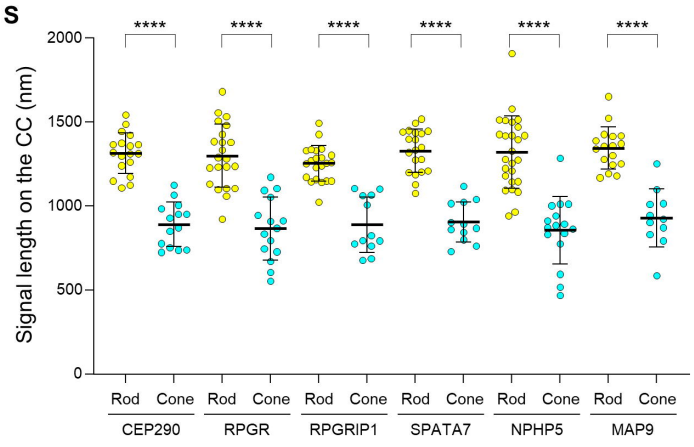
S
Signal length on the CC (nm)
2000
1500
1000
500
0
****
Rod
Cone
CEP290
RPGR
RPGRIP1
SPATA7
NPHP5
MAP9

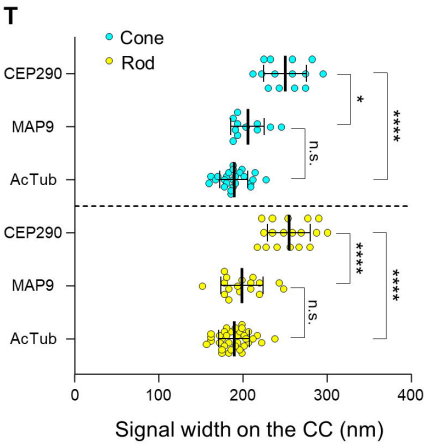
T
Cone
Rod
CEP290
MAP9
AcTub
*
****
n.s.
0
100
200
300
400
Signal width on the CC (nm)

Figure 7

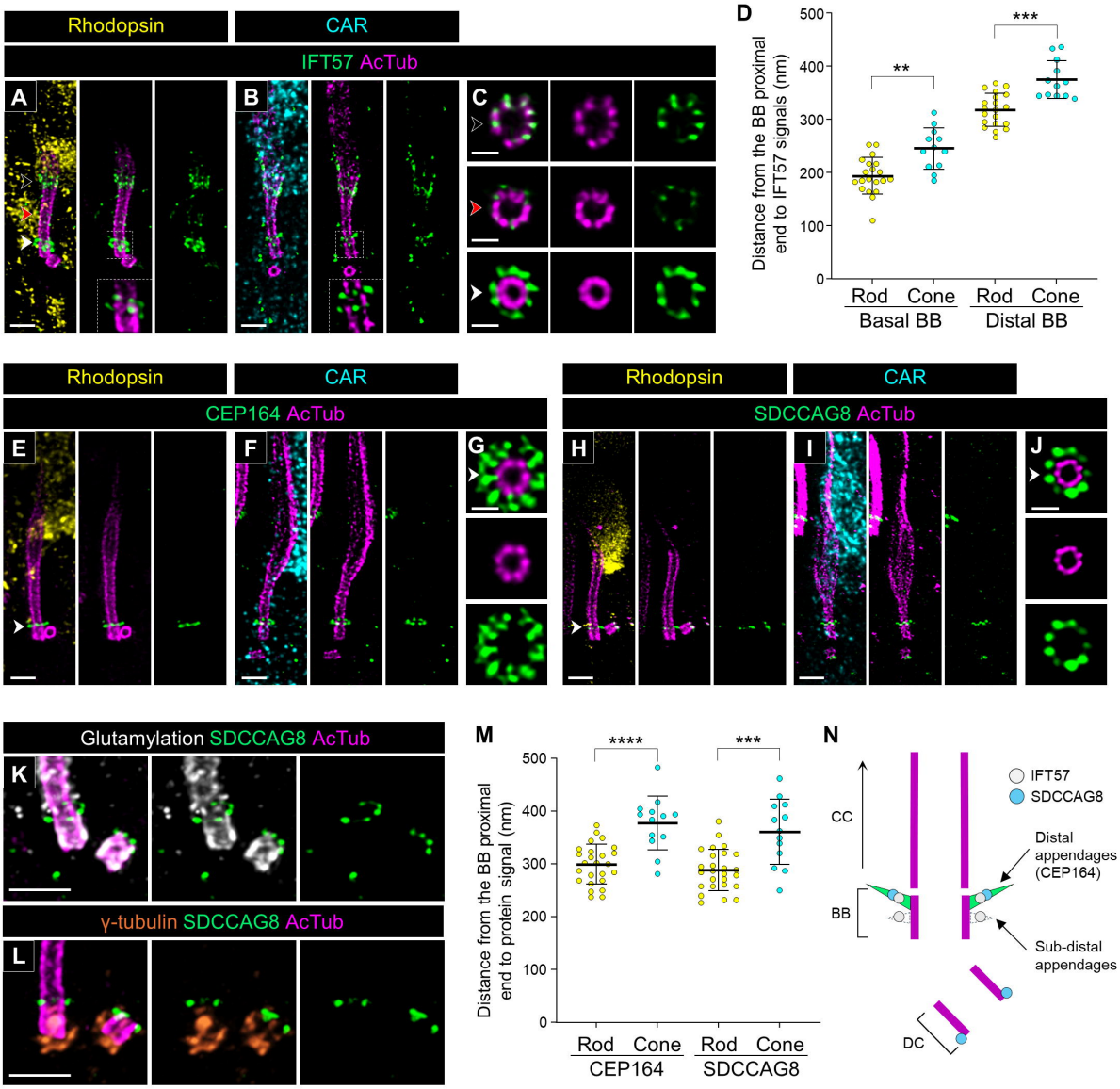
Rhodopsin
CAR
IFT57 AcTub
A
B
C
D
Distance from the BB proximal end to IFT57 signals (nm)
500
400
300
200
100
0
**
***
Rod
Cone
Rod
Cone
Basal BB
Distal BB
Rhodopsin
CAR
CEP164 AcTub
E
F
G
Rhodopsin
CAR
SDCCAG8 AcTub
H
I
J
Glutamylation SDCCAG8 AcTub
K
γ-tubulin SDCCAG8 AcTub
L
M
Distance from the BB proximal end to protein signal (nm)
****
***
Rod
Cone
Rod
Cone
CEP164
SDCCAG8
N
IFT57
SDCCAG8
CC
BB
DC
Distal appendages (CEP164)
Sub-distal appendages

Figure 8

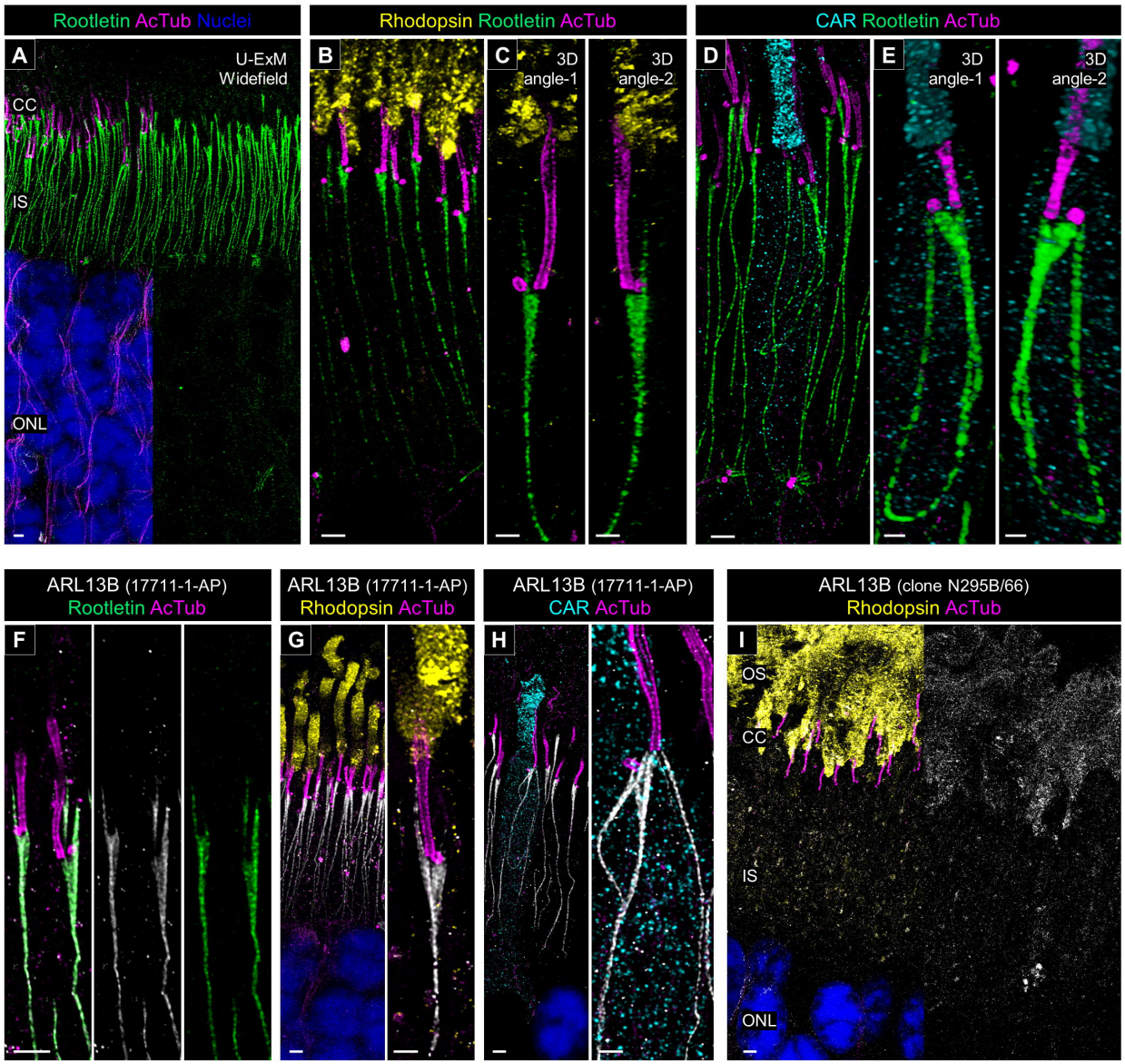
Rootletin AcTub Nuclei
A
U-ExM
Widefield
CC
IS
ONL
Rhodopsin Rootletin AcTub
B
C
3D
angle-1
3D
angle-2
CAR Rootletin AcTub
D
E
3D
angle-1
3D
angle-2
ARL13B (17711-1-AP)
Rootletin AcTub
F
ARL13B (17711-1-AP)
Rhodopsin AcTub
G
ARL13B (17711-1-AP)
CAR AcTub
H
ARL13B (clone N295B/66)
Rhodopsin AcTub
I
OS
CC
IS
ONL

Figure 9

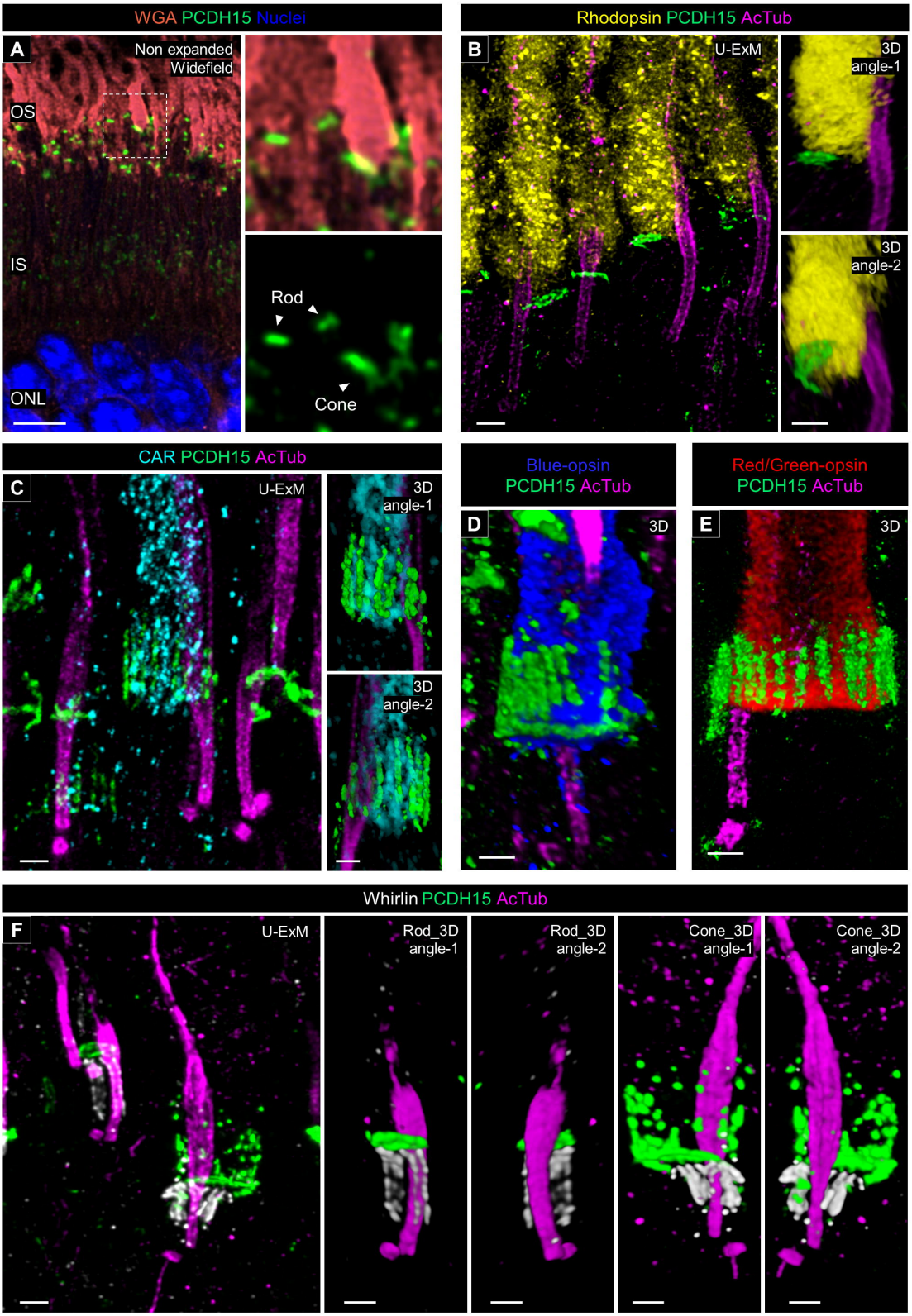
WGA PCDH15 Nuclei
A
Non expanded
Widefield
OS
IS
ONL
Rod
Cone
Rhodopsin PCDH15 AcTub
B
U-ExM
3D
angle-1
3D
angle-2
CAR PCDH15 AcTub
C
U-ExM
3D
angle-1
3D
angle-2
Blue-opsin
PCDH15 AcTub
D
3D
Red/Green-opsin
PCDH15 AcTub
E
3D
Whirlin PCDH15 AcTub
F
U-ExM
Rod_3D
angle-1
Rod_3D
angle-2
Cone_3D
angle-1
Cone_3D
angle-2

Figure 10

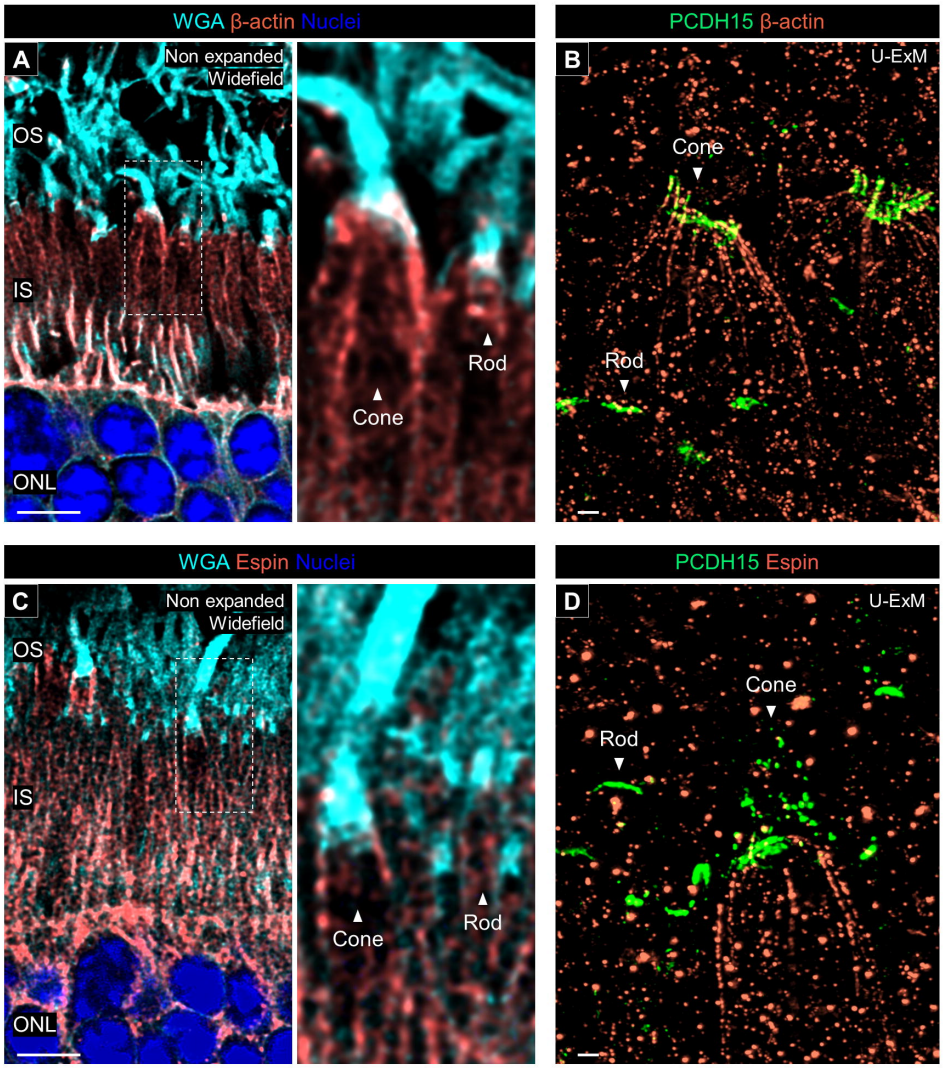
WGA β-actin Nuclei
A
Non expanded
Widefield
OS
IS
ONL
Rod
Cone
PCDH15 β-actin
B
U-ExM
Cone
Rod
WGA Espin Nuclei
C
Non expanded
Widefield
OS
IS
ONL
Cone
Rod
PCDH15 Espin
D
U-ExM
Cone
Rod

Figure 11

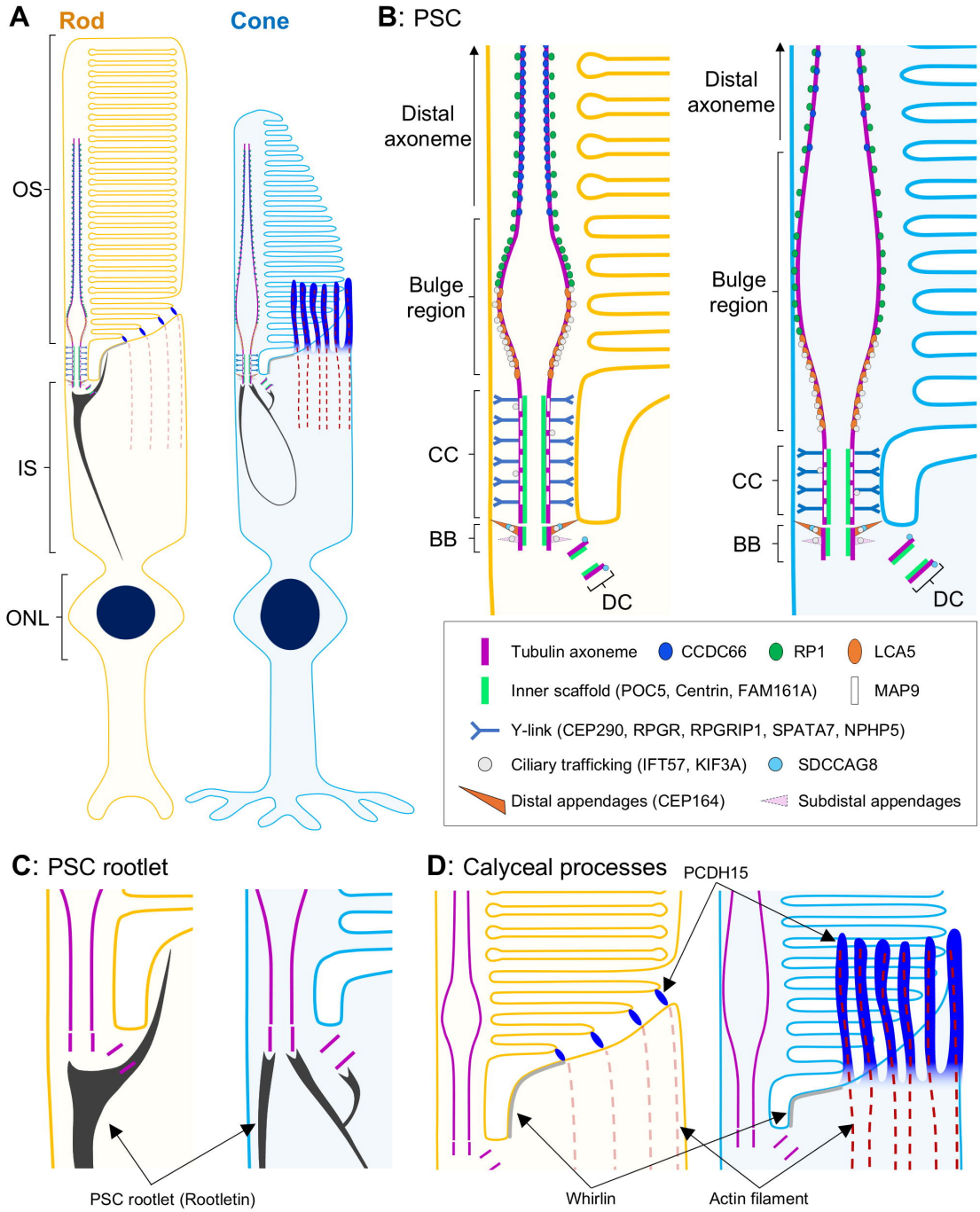
A
Rod
Cone
OS
IS
ONL
B: PSC
Distal axoneme
Bulge region
CC
BB
DC
Tubulin axoneme
CCDC66
RP1
LCA5
Inner scaffold (POC5, Centrin, FAM161A)
MAP9
Y-link (CEP290, RPGR, RPGRIP1, SPATA7, NPHP5)
Ciliary trafficking (IFT57, KIF3A)
SDCCAG8
Distal appendages (CEP164)
Subdistal appendages
C: PSC rootlet
PSC rootlet (Rootletin)
D: Calyceal processes
PCDH15
Whirlin
Actin filament